



Mitochondrial RNA granules are fluid condensates positioned by membrane dynamics

Timo Rey^{1,4}  , Sofia Zaganelli^{1,2,4} , Emilie Cuillery, Evangelia Vartholomaïou² , Marie Croisier³, Jean-Claude Martinou^{1,2}   and Suliana Manley¹  

Mitochondria contain the genetic information and expression machinery to produce essential respiratory chain proteins. Within the mitochondrial matrix, newly synthesized RNA, RNA processing proteins and mitoribosome assembly factors form punctate sub-compartments referred to as mitochondrial RNA granules (MRGs)^{1–3}. Despite their proposed importance in regulating gene expression, the structural and dynamic properties of MRGs remain largely unknown. We investigated the internal architecture of MRGs using fluorescence super-resolution localization microscopy and correlative electron microscopy, and found that the MRG ultrastructure consists of compacted RNA embedded within a protein cloud. Using live-cell super-resolution structured illumination microscopy and fluorescence recovery after photobleaching, we reveal that MRGs rapidly exchange components and can undergo fusion, characteristic properties of fluid condensates⁴. Furthermore, MRGs associate with the inner mitochondrial membrane and their fusion coincides with mitochondrial remodelling. Inhibition of mitochondrial fission or fusion leads to an aberrant accumulation of MRGs into concentrated pockets, where they remain as distinct individual units despite their close apposition. Together, our findings reveal that MRGs are nanoscale fluid compartments, which are dispersed along mitochondria via membrane dynamics.

RNA in eukaryotic and bacterial cells can be sequestered into ribonucleoprotein granules that exhibit a wide range of forms and functions, under both physiological and stress conditions. For example, in the nucleus, speckles and paraspeckles are involved in RNA splicing and transcriptional regulation^{5,6}, whereas the nucleolus creates a compartment for ribosomal assembly^{7,8}. RNA-protein granules often form by liquid–liquid phase separation (LLPS)^{9,10}, and multivalent weak interactions between disordered RNA-binding protein (RBP) domains, and RNA itself, have been identified as hallmark factors for the formation of biomolecular condensates in many *in vitro* and *in silico* studies^{11–13}. However, phase behaviour is sensitive to a number of environmental parameters, such as concentration, ionic strength, pH or crowding, native conditions of which are challenging to reproduce in test tubes¹⁴. Therefore, studies in living cells are fundamental to understanding the formation mechanisms, which may go beyond LLPS¹⁵, and biological functions of such structures.

In mitochondria, mitochondrial RNA granules (MRGs) comprise newly synthesized mitochondrial RNAs (mtRNAs), transcribed from the 16-kb mitochondrial DNA (mtDNA) as long polycistronic precursors, as well as mitochondrial RBPs^{1,2,16}.

It was previously demonstrated that mtRNA is essential for MRG formation³. However, both the structural organization of and the dynamic interplay between MRG components remain unknown. Mitochondria undergo dramatic shape changes through fission, fusion and branching, of which fission directly impacts the distribution of mtDNA^{17,18}. How MRGs respond to this dynamicity and complex architecture is also unknown, due in part to their size (below the diffraction limit). Here, we investigate the molecular organization, distribution and positioning mechanism of MRGs within the mitochondrial network, using super-resolution and correlative fluorescence and electron microscopy. We show that MRGs are ~130-nm, sub-compartmentalized liquid condensates. They associate with the inner mitochondrial membrane (IMM) and mislocalize following perturbation of mitochondrial fission and fusion dynamics.

To assess the MRG dimensions and overall organization, we examined two MRG-associated RBPs—FASTKD2 and GRSF1—along with mtRNA in fixed COS-7 cells. We stained endogenous proteins using immunofluorescence and newly synthesized RNA by incubation with 5 mM bromouridine (BrU) for 1 h, and anti-BrU staining as previously described^{2,3}. In conventional immunofluorescence images against FASTKD2, MRGs appear as bright, diffraction-limited punctae against a dim mitochondrial matrix (Fig. 1a). We used similar fluorescence images to identify in-focus MRGs and the corresponding high-throughput stochastic optical reconstruction microscopy (htSTORM)¹⁹ images to compute their size and shape at the nanoscale (Extended Data Fig. 1). We found that the mtRNA within the MRGs occupied a region with a median diameter of 92 nm (± 40 nm (s.d.), $n = 431$; Fig. 1b and Supplementary Fig. 1). To assess the MRG shape we determined the ratio between the long and short axes for each granule and measured a median eccentricity of 1.7 (± 0.6 s.d.) for mtRNA (Extended Data Fig. 1 and Supplementary Fig. 1). mtDNA is also packaged into punctate structures called nucleoids, which we measured to have a diameter of 88 nm (± 32 nm (s.d.), $n = 310$; Fig. 1b and Supplementary Fig. 2), when stained with antibodies against mtDNA. This is consistent with previous reports of ~100-nm nucleoid diameters^{20–22}, as is our estimated eccentricity of 1.7 (± 0.7 s.d.), reflecting a slightly ellipsoidal shape. Thus, mtDNA serves as an internal reference or positive control for our STORM-based size and shape measurements.

We then quantified the nanostructure of MRGs immunolabelled for GRSF1 or FASTKD2 (bona fide MRG markers), where mutations in the latter are associated with severe mitochondrial diseases^{23,24}. Our measurements showed that the MRG diameter marked by either protein is significantly larger than that of mtRNA: 139 nm

¹Laboratory of Experimental Biophysics, École Polytechnique Fédérale de Lausanne (EPFL), Lausanne, Switzerland. ²Department of Cell Biology, University of Geneva, Genève, Switzerland. ³BioEM Core Facility and Technology Platform, Ecole Polytechnique Fédérale de Lausanne (EPFL), Lausanne, Switzerland.

⁴These authors contributed equally: Timo Rey, Sofia Zaganelli.  e-mail: timo.rey@epfl.ch; jean-claude.martinou@unige.ch; suliana.manley@epfl.ch

(± 36 nm (s.d.), $n=297$) for FASTKD2 and 123 nm (± 31 nm (s.d.), $n=338$) for GRSF1 foci in COS-7 cells (Fig. 1b and Supplementary Figs. 3 and 4). Alternative size descriptors, including radius of gyration and convex hull area, showed the same trends (Extended Data Fig. 1). Furthermore, protein punctae are significantly rounder, with an eccentricity of 1.4 (± 0.4 s.d.) and 1.5 (± 0.5 s.d.) for FASTKD2 and GRSF1, respectively (Extended Data Fig. 1), underlining the differences between RNA and protein organization in MRGs.

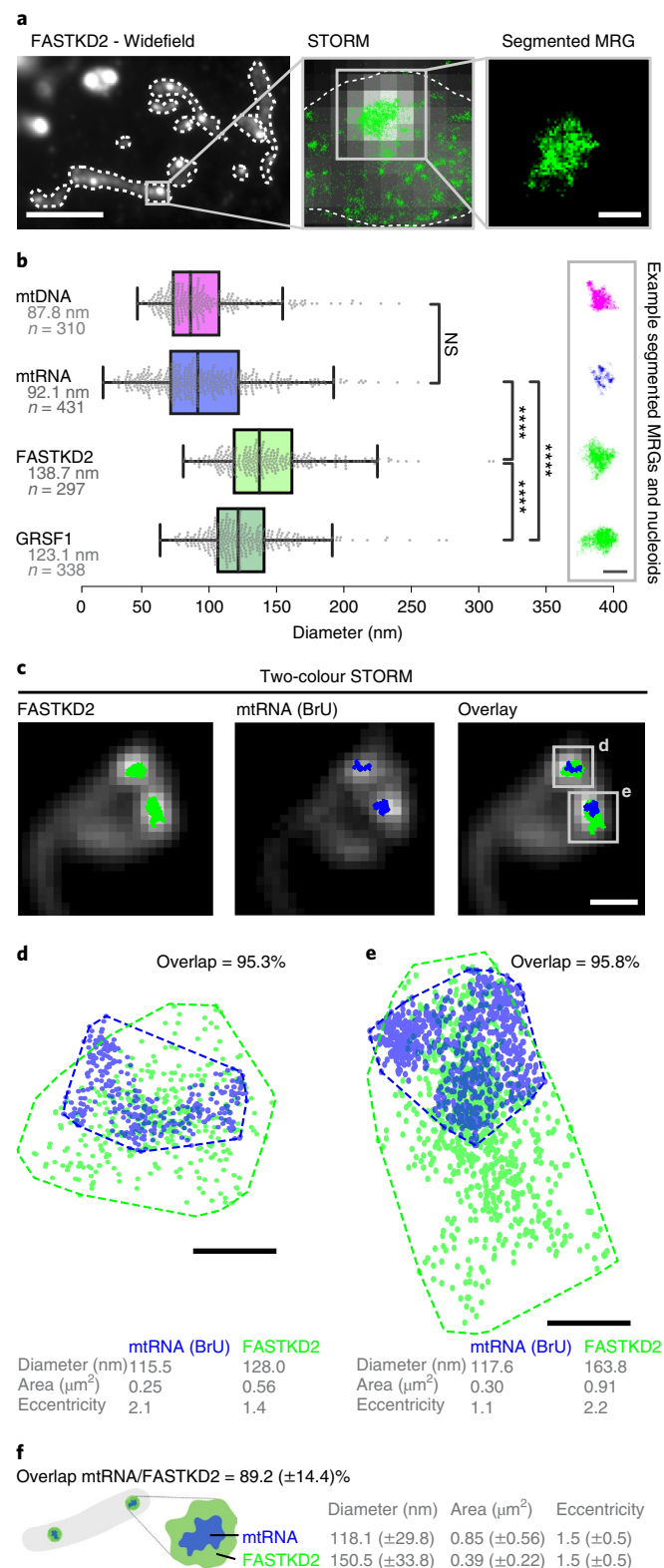
To further investigate the MRG architecture and the relationship between mtRNA- and FASTKD2-foci dimensions, we next performed two-colour htSTORM (Fig. 1c and Extended Data Fig. 2). We found no correlation between the size ($R=0.26$, $n=26$) or eccentricity ($R=0.42$) of the protein components and newly synthesized RNA for individual granules (Extended Data Fig. 2). Yet, in 80% of measured MRGs, the projected area of mtRNA was smaller and contained within ($>80\%$ overlap) the FASTKD2 area (Fig. 1d–f and Supplementary Table 1). These quantifications led us to schematize the ultrastructure of a typical MRG as compacted RNA surrounded by and commingled with RBPs (Fig. 1f).

Liquid phase properties, such as the ability to rapidly exchange components while maintaining a high local concentration of selected molecules, play a functional role in stress and other RNA granules by enabling mRNA sequestration, enzyme buffering and tuning of reaction kinetics⁹. These roles may apply to MRGs and their function in gene expression, if they are indeed liquid-like. To test this hypothesis, we generated stable FASTKD2-eGFP expressing cell lines and assessed the common hallmarks of fluids: content exchange and droplet fusion²⁵. We examined the molecular exchange of MRG components by fluorescence recovery after photobleaching (FRAP). To monitor MRG fluorescence inside highly mobile mitochondria, we developed a software tool for FRAP analysis with motion tracking (Fig. 2a). We found FASTKD2-eGFP molecules within MRGs to recover on average to $\sim 64\%$ of their bleached intensity, with a median half-recovery time of 5.8 s (± 3.3 s (s.d.)) and 4.6 s (± 11.3 s (s.d.)) in U2OS and COS-7 cells, respectively (Fig. 2c,d, Extended Data

Fig. 3 and Supplementary Videos 1 and 2). To test whether dynamic exchange is generalizable beyond FASTKD2, we created two additional stable cell lines expressing MRG markers—ERAL1 and DDX28^{26,27}—both fused to eGFP. Both recovered at a timescale similar to FASTKD2 (half-recovery time of 1.9 s (± 0.7 s (s.d.)) for ERAL1 and 3.1 s (± 1.9 s (s.d.)) for DDX28 (Fig. 2c, Extended Data Fig. 3 and Supplementary Videos 3 and 4). For comparison, we overex-

Fig. 1 | The nanoscopic architecture of MRGs consists of compacted RNA surrounded by RNA binding proteins.

a, Wide-field immunofluorescence of FASTKD2 (left) shows punctate, diffraction-limited MRGs within mitochondria (white dashed lines). Scale bar, 10 μ m. Zoomed view (centre) of a representative MRG: overlay of STORM (green) and wide-field images (greyscale). Right: the MRG is segmented by its high density of STORM localizations (right) using DBSCAN³⁸. Scale bar, 200 nm. The images are representative of the dataset shown in **b**. **b**, MRG (mtRNA, FASTKD2 or GRSF1) and nucleoid (mtDNA) diameters determined as mean full-width at half-maximum (FWHM) from htSTORM images. The numbers (n) of clusters quantified for each condition are shown in the figure and are pooled from 24, 13, 7 and 14 fields of view (FOVs) and 4, 4, 3 and 2 samples for BrU, GRSF1, FASTKD2 and mtDNA, respectively. The median diameter and number of analysed clusters are noted. Box plots denote the first and third quartiles and the median; the whiskers comprise the rest of the distributions, except outliers. A two-sided Mann–Whitney U-test was used and **** denotes P values < 0.0001 ; NS, non-significant ($P_{\text{BrU-mtDNA}} = 1$, $P_{\text{BrU-FASTKD2}} = 1.0 \times 10^{-48}$, $P_{\text{BrU-GRSF1}} = 4.5 \times 10^{-30}$, $P_{\text{GRSF1-FASTKD2}} = 3.1 \times 10^{-11}$). Representative images are shown on the right. Scale bar, 200 nm. **c**, Example of two-colour htSTORM of MRGs (anti-FASTKD2, green) and mtRNA (anti-BrdU, blue) overlaid on wide-field images (grey). Scale bar, 500 nm. Images are representative of the dataset shown in **f**. **d,e**, Scatter plots of localizations from the clusters marked **d** and **e** in **c**. Areas were estimated using a convex hull (dashed line) and used to find the percent overlap between channels. Diameter and eccentricity were also quantified (Supplementary Information). Scale bars, 100 nm. **f**, Schema of MRG organization and median \pm s.d. values for all analysed two-colour htSTORM clusters ($n=26$ MRGs were examined over eight independent experiments). Statistical source data are provided in Source Data Fig. 1.



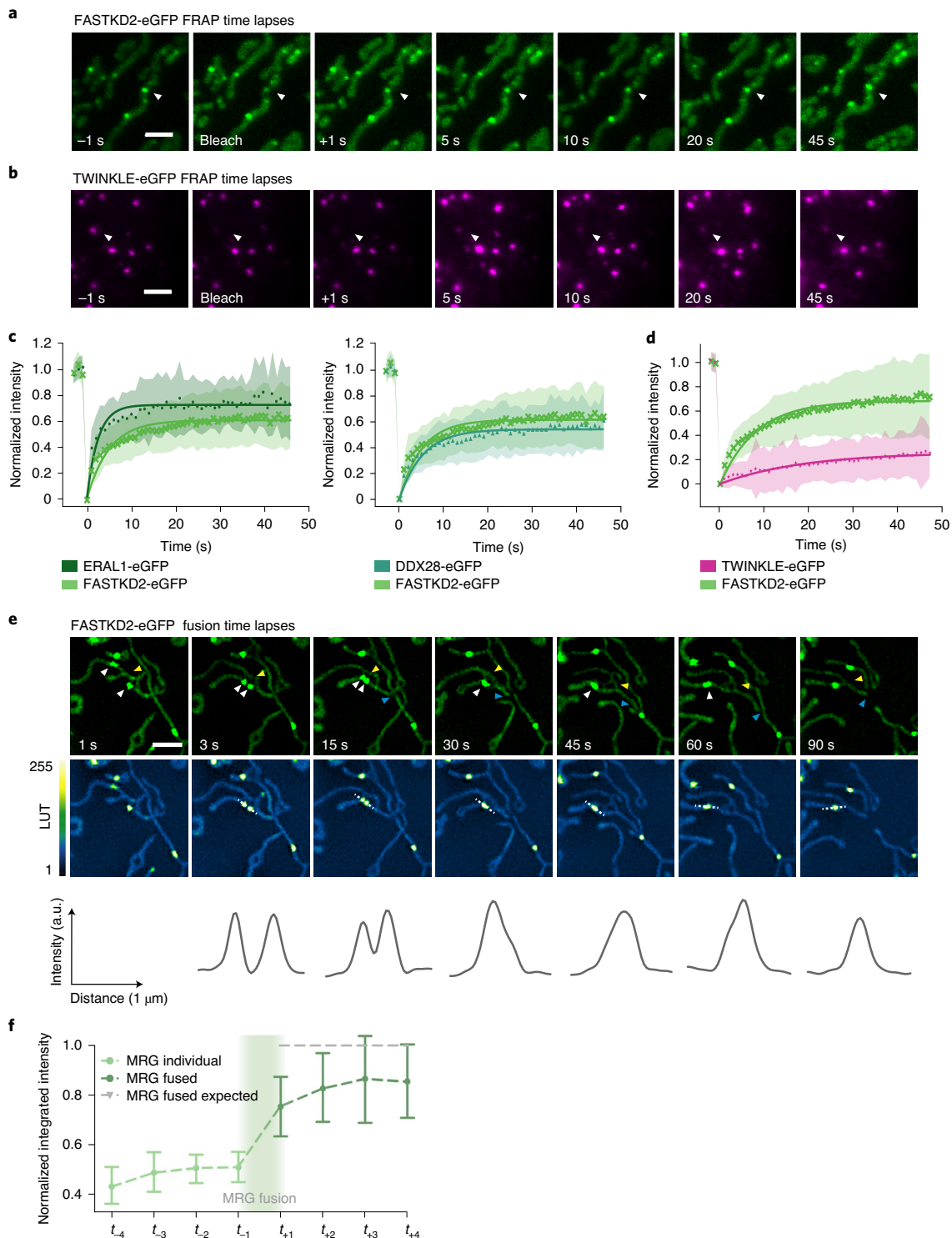


Fig. 2 | MRGs exchange content and undergo fusion in live COS-7 cells. **a, b**, Examples of FRAP time-lapse series of MRGs (**a**, stable expression, FASTKD2-eGFP, green) or nucleoids (**b**, transient transfection, TWINKLE-eGFP, magenta), from the datasets represented in **c** and **d**, respectively. An individual MRG or nucleoid (arrowhead) was partially photobleached to allow tracking during recovery. Scale bars, 2 μm . **c, d**, FRAP intensity, where symbols represent mean data points, lines are single exponential fits, and shaded areas are standard deviations at each time point, for FASTKD2-eGFP ($n=44$ MRGs examined over eight independent experiments) and ERAL1-eGFP ($n=17$ MRGs examined over three independent experiments), DDX28-eGFP ($n=17$ MRGs examined over three independent experiments) (**c**) and TWINKLE-eGFP ($n=50$ nucleoids examined over five independent experiments) (**d**). **e**, Representative SIM time-lapse series of an MRG fusion event (white arrowheads) in cells stably expressing FASTKD2-eGFP. Cells were imaged at 1/3 Hz. Yellow and blue arrowheads highlight mitochondrial network dynamics (top). MRGs enriched in FASTKD2-eGFP stand out in yellow; pixel intensity values are shown with a linear Fire lookup table (LUT). Line profiles of MRGs along the mitochondrial axis (middle, dashed lines) show the intensity values at each time point (bottom). Scale bar, 2 μm . **f**, Temporal evolution of the integrated intensity of MRGs in COS-7 cells before and after fusion. Pre-fusion integrated intensities were summed for each granule pair ($n=9$ biologically independent cells) and the sums were used for normalization (grey dashed line). Data are presented as mean and s.d. for each MRG type for four time points before fusion (light green, t_{-4} – t_{-1}) as well as after fusion (dark green, t_{+1} – t_{+4}). Statistical source data are provided in Source Data Fig. 2.

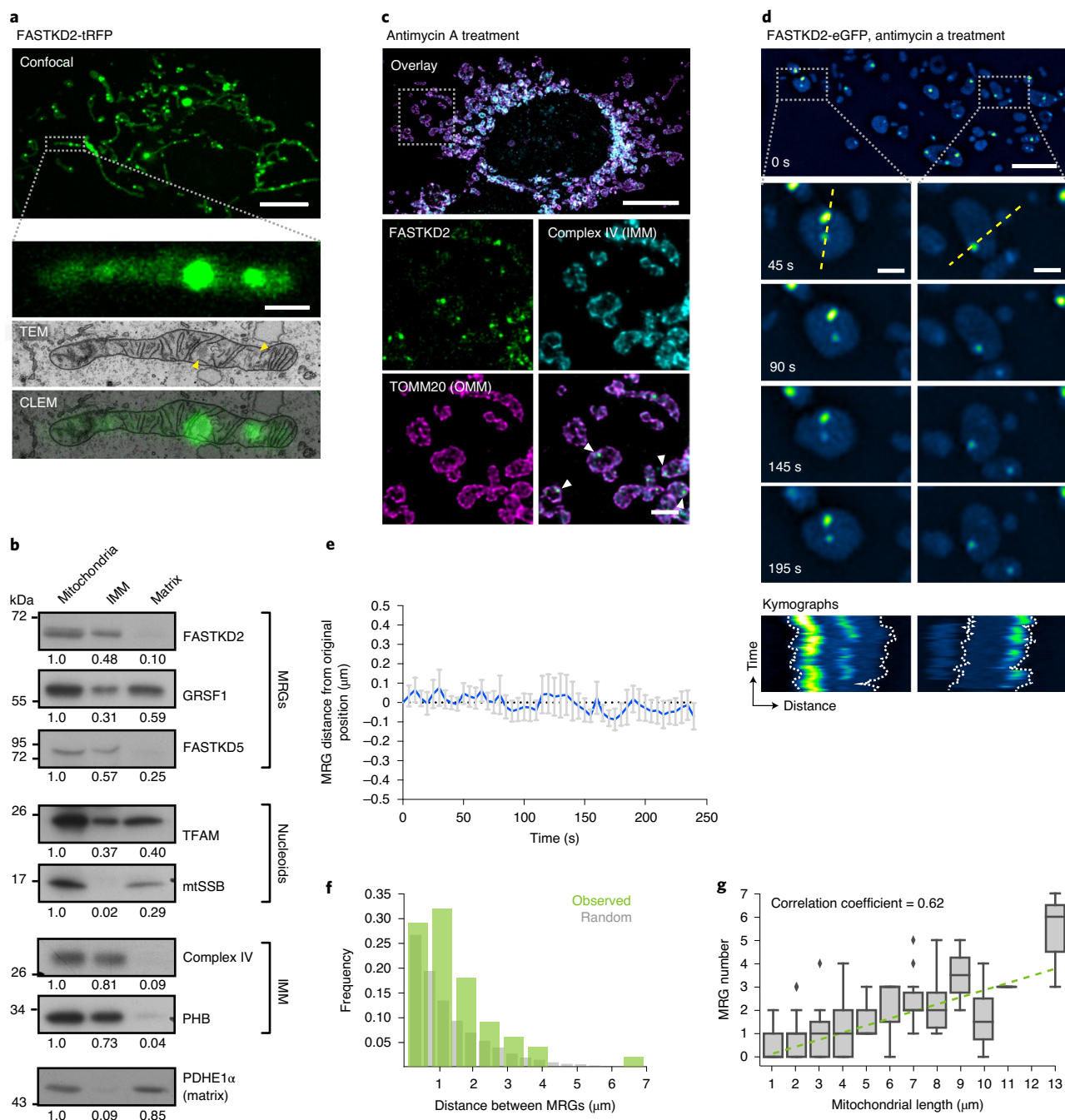


Fig. 3 | MRGs are associated with inner mitochondrial membranes and are randomly spaced along the mitochondrial network. **a**, Correlated fluorescence (axially projected confocal image, green) and transmission electron micrograph (TEM, greyscale), in a FASTKD2-tRFP expressing COS-7 cell. Electron densities corresponding to MRGs are visible (arrowheads; $n=7$ MRGs from three mitochondria). Scale bars, $10\ \mu\text{m}$ (top) and $1\ \mu\text{m}$ (bottom). **b**, Western blot of fractionated mitochondria, probed with antibodies against MRG (FASTKD2, GRSF1, FASTKD5) and nucleoid (transcription factor A, mitochondrial (TFAM), mtSSB) components. IMM-integrated proteins (complex IV, prohibitin (PHB)) and soluble matrix protein pyruvate dehydrogenase E1 α (PDHE1 α) served as controls. Blots were processed simultaneously and compared quantitatively from the same gel. The experiment was performed twice with similar results. **c**, FASTKD2-eGFP expressing HeLa cells treated with $100\ \mu\text{M}$ antimycin A for 1 h, then fixed. IMM (anti-complex IV, cyan) and outer mitochondrial membrane (OMM, anti-TOMM20, magenta), reveal swollen mitochondria with few inner membranes. MRGs appear proximal to the IMM (arrowheads). The experiment was performed twice with similar results. Scale bars, $10\ \mu\text{m}$ (top), $2\ \mu\text{m}$ (bottom). **d**, FASTKD2-eGFP expressing COS-7 cells treated with $100\ \mu\text{M}$ antimycin A for 1 h, imaged live. Pixel intensity values are shown with a linear Fire LUT as in Fig. 2e. Time-lapse series are shown for two exemplary mitochondria (dashed boxes). Kymographs (from the yellow dashed line) highlight the co-mobility of individual granules. Scale bars, $10\ \mu\text{m}$ (top) and $1\ \mu\text{m}$ (bottom). The experiment was performed twice with similar results. **e**, MRG movement over time, measured as the distance between the MRG and the closest membrane, for swollen mitochondria as exemplified in **d** ($n=20$ MRGs examined from three cells). Data are presented as mean (blue line) \pm s.d. (error bars). **f**, Histogram of the distance between neighbouring pairs of MRGs for unbranched mitochondria ($n=100$ mitochondria over three independent experiments, green) and simulated randomly distributed granules (grey). **g**, Correlation between MRG number and length of unbranched mitochondria ($n=206$ mitochondria over three independent experiments). Each box plot denotes the median and first and third quartiles, and diamonds show outliers for each bin (for example, bin₁=0–1 μm and so on). The linear regression (green dashed line) was computed on non-binned data. Unprocessed blots and statistical source data are provided in Source Data Fig. 3.

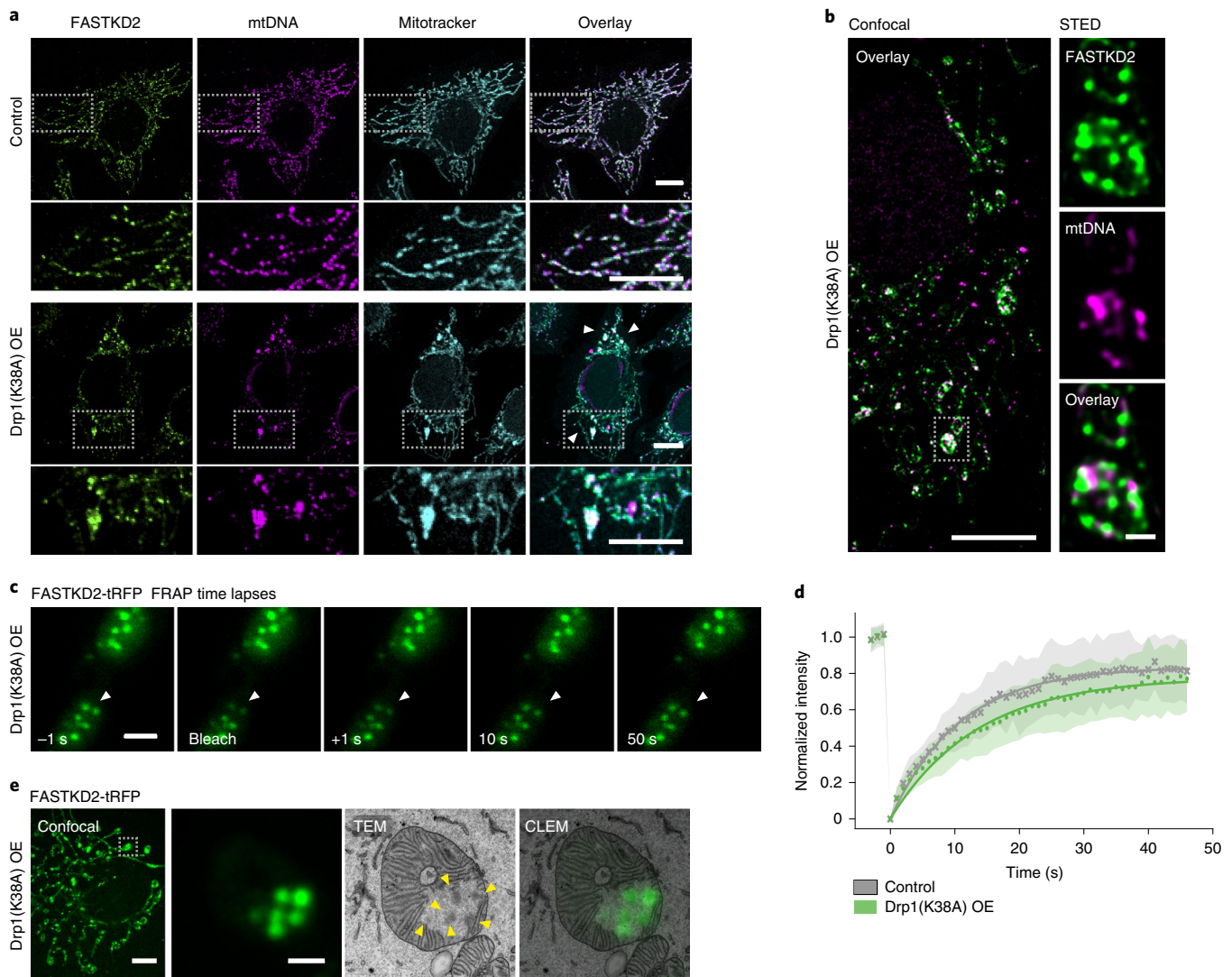


Fig. 4 | Impaired mitochondrial fission leads to aberrant MRG positioning. **a**, HeLa cells imaged by confocal microscopy in control settings (top) or after 48 h of Drp1^{K38A} overexpression (OE, bottom), stained for MRGs (anti-FASTKD2, green), nucleoids (anti-DNA, magenta) and mitochondria (MitoTracker Deep Red, cyan). The second and fourth rows show zoomed views of the regions indicated by grey boxes in the first and third rows. The experiment was performed three times with similar results. Scale bars, 10 μ m (first and third rows) and 1 μ m (second and fourth rows). **b**, Confocal (left) and STED (right) images of mito-bulbs containing MRGs (anti-FASTKD2, green) and nucleoids (anti-mtDNA, magenta) in fixed Drp1^{K38A}-overexpressing COS-7 cells. The experiment was performed twice with similar results. Scale bars, 10 μ m (left) and 2 μ m (right, zoom). **c**, Example of FRAP time-lapse images from the datasets represented in **d** of mito-bulb-associated MRGs (arrowheads), in FASTKD2-tRFP (green) stably expressing COS-7 cells transiently transfected with Drp1^{K38A} for 24 h. Scale bar, 2 μ m. **d**, Comparison of FASTKD2-tRFP FRAP between control ($n=31$ MRGs examined over four independent experiments) and Drp1^{K38A} ($n=40$ MRGs examined over three independent experiments) overexpressing cells. Symbols represent mean data points, lines are single exponential fits and shaded areas are s.d. values for each time point. **e**, Confocal fluorescence and TEM (CLEM) of MRGs (stable expression, FASTKD2-tRFP, green) in COS-7 cells, fixed 24 h after Drp1^{K38A} transfection. Zoom of a single mitochondrion shows several MRGs (arrowheads), resembling a bunch of grapes (10 MRGs were analysed from three mitochondria). Scale bars, 10 μ m (left), 1 μ m (right). Grey dashed boxes indicate magnified regions. Statistical source data are provided in Source Data Fig. 4.

pressed the mitochondrial helicase TWINKLE fused to eGFP as a nucleoid marker with high DNA-binding affinity²⁸. TWINKLE foci only slightly (~29%) recovered over the course of our FRAP assay (50 s), and served as negative control to highlight that fast protein exchange is particular to MRGs (Fig. 2b,d). Thus, MRG components exchange rapidly, on a fast timescale, even compared to stress granules (recovery half-time, 18.5–35 s)²⁹.

Whereas liquid drops may fuse upon contact, solid granules will instead remain inert or aggregate while maintaining their shape. We followed FASTKD2 foci by live-cell super-resolved structured illumination microscopy (SIM), which provides the necessary reso-

lution to discern the two cases. We observed MRG fusion in multiple instances in both U2OS and COS-7 cells, where two individual foci merged to form a single spot (Fig. 2e, Extended Data Fig. 4 and Supplementary Videos 5 and 6). We also noted MRG splitting on some occasions (Extended Data Fig. 4 and Supplementary Video 7). Imaging TWINKLE-eGFP by SIM, we observed nucleoid 'kiss-and-runs' and nucleoid splitting, as previously described³⁰, as well as one fusion event (Extended Data Fig. 4 and Supplementary Videos 8 and 9). We determined the photobleaching-corrected integrated intensity of FASTKD2-eGFP in the merged droplet to be approximately the sum of the initial droplets, as expected if no

material was lost during fusion (Fig. 2f). Notably, 75% of fusion events coincided with visible mitochondrial rearrangements such as fusion, fission or bulging (Supplementary Table 2).

Infoldings of the IMM called cristae densely populate the mitochondrial interior. By correlative fluorescence and electron microscopy (CLEM), we observed that displaced cristae accommodate MRGs in open spaces (Fig. 3a), as was recently reported for nucleoids by live-cell stimulated emission depletion (STED) microscopy³¹. MRGs are clearly distinguishable as round electron-dense granules, with dimensions consistent with our htSTORM data (Figs. 1 and 3a and Extended Data Fig. 5) and an ultrastructure reminiscent of that of stress granules and P-bodies³².

Noticing their close proximity to the IMM and intrigued by the concurrence between MRG fusion and membrane dynamics, we assessed their association with the membrane using both biochemical and image-based approaches. First, we performed a biochemical fractionation to enrich for IMM or matrix-associated proteins. We found MRG components FASTKD2 and FASTKD5 primarily in the IMM fraction, while GRSF1 was present in both IMM and matrix fractions (Fig. 3b), similar to the nucleoid associated protein TFAM, in accordance with previous reports³³. Next, we swelled mitochondria by antimycin A treatment of live COS-7 and HeLa cells to test whether MRGs would diffuse freely within the cristae-devoid enlarged lumen³⁴ or remain associated with the IMM. We observed that most MRGs decorated the perimeter (Fig. 3c) and retained their relative position within mitochondria over time (Fig. 3d,e, Extended Data Fig. 6 and Supplementary Videos 10 and 11), consistent with IMM association. Thus, as nucleoids³³, MRGs appear to be physically attached to the IMM.

We then assessed the distribution of MRGs along the mitochondrial network. A semiregular nucleoid spacing was found to be important in fission yeast to circumvent the problem that random spacing would contribute to binomial errors in genome partitioning and thus a high probability of total mtDNA loss¹⁷. We used the same method to compare measured inter-MRG distances with those of simulated randomly placed granules (Fig. 3f). Our analysis shows that the positions of individual MRGs within their respective mitochondria are not distinguishable from a random distribution (Extended Data Fig. 6), while the distances between MRGs inside the same mitochondrion are at the borderline of being considered different from random ($P=0.04997$; Fig. 3f). In the case of a random distribution along the entire mitochondrial network, we would expect an equal probability of finding an MRG anywhere along the network, so that larger mitochondria should have more granules. Indeed, we found on average one MRG for every of $2.00\ \mu\text{m}$ ($\pm 1.65\ \mu\text{m}$) of mitochondria ($n=131$) and a positive correlation between MRG number and mitochondrial length (correlation coefficient=0.62; Fig. 3g and Extended Data Fig. 6). Although nucleoids are accurately positioned¹⁸, our data suggest that MRGs are not.

Because MRGs appear relatively immobile within the matrix, yet are randomly distributed, we decided to investigate the interplay between MRG positioning and mitochondrial dynamics. We inhibited mitochondrial fission by overexpression of a dominant negative mutant of the fission factor dynamin-related protein 1 (Drp1), Drp1^{K38A}. Under this condition, we observed highly elongated mitochondria with enlarged domains, as previously described and termed 'mito-bulbs'³⁵. We found that these domains contain not only nucleoids, but also MRGs (Fig. 4a). With super-resolved STED microscopy, we discovered that mito-bulbs are better described as resembling bunches of grapes, composed of many interspersed MRGs and nucleoids, rather than as a single enlarged and coalesced structure as previously proposed³⁵ (Fig. 4b). Intrigued by the absence of MRG fusion (illustrated in Fig. 2) in such a confined space, we assessed whether MRGs may have solidified, as stress granules can³⁶. We found that fluorescence recovery of stably expressed FASTKD2-tRFP was similar in control and Drp1^{K38A}-overexpressing

cells, suggesting that the liquid nature of MRGs within the mito-bulbs had not changed (Fig. 4c,d and Supplementary Videos 12 and 13). Using CLEM, we confirmed that the MRGs remained as distinct individual units, despite their close apposition, and did not observe the presence of cristae that could have formed physical barriers to the fusion of these granules (Fig. 4e and Extended Data Fig. 5). Furthermore, this EM analysis showed that a number of these electron-dense granules were closely apposed to membranes, consistent with the results shown in Fig. 3a–c. Tightly stacked cristae could be seen adjacent to mito-bulbs in affected mitochondria (Fig. 4d). Knockdown of mitochondrial fusion factor Mitofusin 2 (Mfn2) evoked similar MRG clustering, further supporting a role for mitochondrial dynamics in maintaining an even distribution of MRGs along mitochondria (Extended Data Fig. 7).

In conclusion, our data show that MRGs share several properties with phase-separated condensates, albeit the exact mechanism of their formation is not yet fully elucidated. We propose that condensation of mtRNA and RBPs into MRGs may allow mammalian cells to regulate positioning of these components along the mitochondrial network via membrane association (Fig. 3). Mitochondrial dynamics via fission and fusion is critical for maintaining a random positioning of MRGs, and its perturbation leads to their accumulation in small domains, while their individual stability and capacity for molecular exchange is maintained (Fig. 4). Our findings show that changes in positioning can arise, decoupled from changes in the biophysical properties of RNA sub-compartments. This insight could be important for understanding mitochondrial disorders that are reported to feature aberrant mitochondrial RNA and DNA distribution into clusters. Adequate positioning of genetic material and transcripts may be crucial for proper synthesis of the respiratory chain and oxidative phosphorylation³⁷.

Online content

Any methods, additional references, Nature Research reporting summaries, source data, extended data, supplementary information, acknowledgements, peer review information; details of author contributions and competing interests; and statements of data and code availability are available at <https://doi.org/10.1038/s41556-020-00584-8>.

Received: 13 August 2019; Accepted: 25 August 2020;

Published online: 28 September 2020

References

- Antonicka, H., Sasarman, F., Nishimura, T., Paupe, V. & Shoubridge, E. A. The mitochondrial RNA-binding protein GRSF1 localizes to RNA granules and is required for posttranscriptional mitochondrial gene expression. *Cell Metab.* **17**, 386–398 (2013).
- Iborra, F. J., Kimura, H. & Cook, P. R. The functional organization of mitochondrial genomes in human cells. *BMC Biol.* **2**, 9 (2004).
- Jourdain, A. A. et al. GRSF1 regulates RNA processing in mitochondrial RNA granules. *Cell Metab.* **17**, 399–410 (2013).
- Hyman, A. A., Weber, C. A. & Jülicher, F. Liquid–liquid phase separation in biology. *Annu. Rev. Cell Dev. Biol.* **30**, 39–58 (2014).
- Handwerker, K. E., Cordero, J. A. & Gall, J. G. Cajal bodies, nucleoli and speckles in the *Xenopus* oocyte nucleus have a low-density, sponge-like structure. *Mol. Biol. Cell* **16**, 202–211 (2005).
- Yamazaki, T. et al. Functional domains of NEAT1 architectural lncRNA induce paraspeckle assembly through phase separation. *Mol. Cell* **70**, 1038–1053 (2018).
- Feric, M. et al. Coexisting liquid phases underlie nucleolar subcompartments. *Cell* **165**, 1686–1697 (2016).
- Frottin, F. et al. The nucleolus functions as a phase-separated protein quality control compartment. *Science* **365**, 342–347 (2019).
- Banani, S. F., Lee, H. O., Hyman, A. A. & Rosen, M. K. Biomolecular condensates: organizers of cellular biochemistry. *Nat. Rev. Mol. Cell Biol.* **18**, 285–298 (2017).
- Boeynaems, S. et al. Protein phase separation: a new phase in cell biology. *Trends Cell Biol.* **28**, 420–435 (2018).
- Langdon, E. M. et al. mRNA structure determines specificity of a polyQ-driven phase separation. *Science* **360**, 922–927 (2018).

12. Maharana, S. et al. RNA buffers the phase separation behavior of prion-like RNA binding proteins. *Science* **360**, 918–921 (2018).
13. Wang, J. et al. A molecular grammar governing the driving forces for phase separation of prion-like RNA binding proteins. *Cell* **174**, 688–699 (2018).
14. Alberti, S., Gladfelter, A. & Mittag, T. Considerations and challenges in studying liquid–liquid phase separation and biomolecular condensates. *Cell* **176**, 419–434 (2019).
15. McSwiggen, D. T. et al. Evidence for DNA-mediated nuclear compartmentalization distinct from phase separation. *eLife* **8**, e47098 (2019).
16. Jourdain, A. A. et al. A mitochondria-specific isoform of FASTK is present in mitochondrial RNA granules and regulates gene expression and function. *Cell Rep.* **10**, 1110–1121 (2015).
17. Jajoo, R. et al. Accurate concentration control of mitochondria and nucleoids. *Science* **351**, 169–172 (2016).
18. Lewis, S. C., Uchiyama, L. F. & Nunnari, J. ER-mitochondria contacts couple mtDNA synthesis with mitochondrial division in human cells. *Science* **353**, aaf5549 (2016).
19. Douglass, K. M., Sieben, C., Archetti, A., Lambert, A. & Manley, S. Super-resolution imaging of multiple cells by optimized flat-field epi-illumination. *Nat. Photon.* **10**, 705–708 (2016).
20. Alán, L., Špaček, T. & Ježek, P. Delaunay algorithm and principal component analysis for 3D visualization of mitochondrial DNA nucleoids by Biplane FPALM/dSTORM. *Eur. Biophys. J.* **45**, 443–461 (2016).
21. Brown, T. A. et al. Superresolution fluorescence imaging of mitochondrial nucleoids reveals their spatial range, limits and membrane interaction. *Mol. Cell. Biol.* **31**, 4994–5010 (2011).
22. Kukat, C. et al. Super-resolution microscopy reveals that mammalian mitochondrial nucleoids have a uniform size and frequently contain a single copy of mtDNA. *Proc. Natl Acad. Sci. USA* **108**, 13534–13539 (2011).
23. Ghezzi, D. et al. FASTKD2 nonsense mutation in an infantile mitochondrial encephalomyopathy associated with cytochrome c oxidase deficiency. *Am. J. Hum. Genet.* **83**, 415–423 (2008).
24. Yoo, D. H. et al. Identification of FASTKD2 compound heterozygous mutations as the underlying cause of autosomal recessive MELAS-like syndrome. *Mitochondrion* **35**, 54–58 (2017).
25. Brangwynne, C. P. et al. Germline P granules are liquid droplets that localize by controlled dissolution/condensation. *Science* **324**, 1729–1732 (2009).
26. Tu, Y. T. & Barrientos, A. The human mitochondrial DEAD-Box protein DDX28 resides in RNA granules and functions in mitoribosome assembly. *Cell Rep.* **10**, 854–864 (2015).
27. Zaganelli, S. et al. The pseudouridine synthase RPUSD4 is an essential component of mitochondrial RNA granules. *J. Biol. Chem.* **292**, 4519–4532 (2017).
28. Farge, G. et al. The N-terminal domain of TWINKLE contributes to single-stranded DNA binding and DNA helicase activities. *Nucleic Acids Res.* **36**, 393–403 (2008).
29. Wheeler, J. R., Matheny, T., Jain, S., Abrisch, R. & Parker, R. Distinct stages in stress granule assembly and disassembly. *eLife* **5**, e18413 (2016).
30. Garrido, N. et al. Composition and dynamics of human mitochondrial nucleoids. *Mol. Biol. Cell* **14**, 1583–1596 (2003).
31. Stephan, T., Roesch, A., Riedel, D. & Jakobs, S. Live-cell STED nanoscopy of mitochondrial cristae. *Sci. Rep.* **9**, 12419 (2019).
32. Souquere, S. et al. Unravelling the ultrastructure of stress granules and associated P-bodies in human cells. *J. Cell Sci.* **122**, 3619–3626 (2009).
33. Gerhold, J. M. et al. Human mitochondrial DNA–protein complexes attach to a cholesterol-rich membrane structure. *Sci. Rep.* **5**, 15292 (2015).
34. Hytti, M. et al. Antimycin A-induced mitochondrial damage causes human RPE cell death despite activation of autophagy. *Oxid. Med. Cell. Longev.* **2019**, 1583656 (2019).
35. Ban-Ishihara, R., Ishihara, T., Sasaki, N., Mihara, K. & Ishihara, N. Dynamics of nucleoid structure regulated by mitochondrial fission contributes to cristae reformation and release of cytochrome c. *Proc. Natl Acad. Sci. USA* **110**, 11863–11868 (2013).
36. Jain, S. et al. ATPase-modulated stress granules contain a diverse proteome and substructure. *Cell* **164**, 487–498 (2016).
37. Durigon, R. et al. LETM1 couples mitochondrial DNA metabolism and nutrient preference. *EMBO Mol. Med.* **10**, e8550 (2018).
38. Ester, M., Kriegel, H.-P., Sander, J. & Xu, X. A density-based algorithm for discovering clusters in large spatial databases with noise. In *Proceedings of the 2nd International Conference on Knowledge Discovery and Data Mining* 226–231 (AAAI, 1996).

Publisher's note Springer Nature remains neutral with regard to jurisdictional claims in published maps and institutional affiliations.

© The Author(s), under exclusive licence to Springer Nature Limited 2020

Methods

Plasmids and reagents. All cell culture reagents and chemicals were purchased from Sigma unless stated otherwise.

The following plasmids were cloned in the laboratory, using pWPT lentiviral vector (Addgene 12255) as a backbone: FASTKD2-eGFP, FASTKD2-tRFP, DDX28-eGFP, ERAL1-eGFP and TWINKLE-eGFP. CFP-Drp1(K38A) plasmid was a gift from A. Van der Bliek. Plasmids for lentiviral production pMD2.G and psPAX2 were gifts from D. Trono (Addgene 12259 and 12260, respectively).

Cell culture and transfection. HeLa (ATCC, CCL-2), HEK293T (ATCC, CRL-11268), COS-7 (ECACC, 87021302) and U2OS (ATCC, HTB-96) cells were cultured in 5% CO₂ at 37°C in Dulbecco's modified Eagle medium (DMEM) supplemented with 10–25 mM glucose, 4 mM GlutaMAX (Gibco) or 2 mM L-glutamine, 10% heat-inactivated fetal bovine serum (FBS), 100 U ml⁻¹ penicillin and 100 mg ml⁻¹ streptomycin. All cells were maintained in culture for a maximum of 20 passages, and routinely assessed for mycoplasma contamination. CRISPR-engineered HeLa Cox8a-SNAP cells were a gift from T. Stephan and S. Jakobs³¹.

Plasmid transfection of cells was performed using Lipofectamine LTX (Invitrogen) or FuGENE 6 (Promega) according to the manufacturer's instructions (typically 4–6 µl FUGENE reagent and 100–500 ng of plasmid DNA were used per well of a six-well plate). Cells were analysed 12–48 h after transfection. siRNA transfection was performed using Lipofectamine RNAi Max (Invitrogen) and cells were analysed 72 h after transfection.

For Drp1 and Mfn2 silencing, ON-TARGETplus SMARTpool (Dharmacon, GE Healthcare) were used following the manufacturer's instructions (siDrp1, cat. no. L-012092-00; siMfn2, cat. no. L-012961-00; ON-TARGETplus non-targeting pool (negative control), cat. no. D-001810-10).

Stable cell line generation. We used a second-generation lentiviral system to transform individual cell lines. In brief, gene sequences of interest were cloned into lenti-expression vector pWPT (as described above). Co-transfection of HEK293T cells was performed with packaging plasmids pMD2.G and psPAX2 using calcium phosphate precipitation. Medium containing virus was collected 48 h after transfection and filtered using membranes with a pore size of 0.45 µm. The viral supernatant and polybrene were added to 70% confluent recipient cells, and culture medium was replaced 24 h after infection. For FASTKD2-, ERAL1- and DDX28-eGFP cell lines, FACS sorting was performed with the help of the Flow Cytometry Core Facility at EPFL, to enrich cells expressing eGFP at the desired level.

Live-cell treatments. Bromouridine tagging of RNA. When a bromouridine pulse assay was performed, cells were incubated with 5 mM 5-bromouridine (BrU) in complete culture medium for 1 h before fixation, as previously described³². BrU was stored at –20°C as 250 mM aliquots, and was heated and vortexed before dilution in culture medium when used.

Antimycin A treatment. For antimycin A treatment, cells were incubated with 25 or 100 µM antimycin A (Abcam) in complete culture medium for 24 h or 1 h, respectively, before fixation or live imaging. Live imaging was performed in Leibovitz L-15 medium (Gibco) for SIM microscopy or Live Cell Imaging Solution (Thermo Fisher Scientific) for STED microscopy, supplemented with adequate amount of antimycin A. Antimycin A was resuspended in EtOH at 1 mM and stored at –20°C.

Immunofluorescence. Cells were seeded on glass coverslips and grown to a confluence of 40–80%. Following live-cell treatments if indicated, fixation of cultured cells was performed in warm 4% paraformaldehyde (PFA) in phosphate-buffered saline (PBS) for 15 min. Then, cells were rinsed with PBS, and cell permeabilization and blocking were co-executed by incubating the fixed cells in PBS containing 0.3% Triton X-100 and 10% pre-immune goat serum for 15 min. The same buffer was used to incubate cells with the specified primary antibody (see antibody list below). After incubation with primary antibodies overnight in a humid chamber and at 4°C or 2 h at room temperature, the cells were washed with PBS and incubated with the appropriate secondary antibody conjugated with a fluorophore. Where indicated, the mitochondrial network was stained before fixing the cells using MitoTracker Deep Red FM (Thermo Fisher Scientific), according to the manufacturer's instructions.

Antibodies used for immunofluorescence. The following primary antibodies were used for immunofluorescence: anti-FASTKD2 (Proteintech, 17464-1-AP; 1:250 dilution), anti-bromodeoxyuridine (Roche, 11170376001; 1:250 to 1:500 dilution), anti-GRSF1 (Sigma, HPA036985; 1:250 dilution), anti-DNA (ProGen, 61014; 1:250 to 1:400 dilution), anti-TOMM20 (Abcam, ab186734; Santa Cruz Biotech, SC-17764; 1:200 dilution for both antibodies), anti-OxPhos Complex IV subunit IV (clone 20E8C12, Thermo Fisher Scientific, A21348; 1:200 dilution) and anti-mtHSP70 (Thermo Fisher Scientific, MA3-028; 1:250 dilution).

The secondary antibodies differed depending on the microscopy technique applied and are detailed in the following. All secondary antibodies for immunofluorescence were diluted 1:500–1:1,000.

htSTORM. htSTORM experiments were performed as previously described^{19,39}, using the same hardware. Microscope acquisitions were controlled by Micromanager software (v. 2.0 beta), interfaced with the Thorlabs APT software (v. 3.21.4) to control the piezo stage. Immunofluorescence was performed as described above. The following primary antibodies were combined for one- or two-colour imaging, as stated in the figures: anti-FASTKD2, anti-bromodeoxyuridine, anti-GRSF1 and anti-DNA. For one-colour htSTORM we used Alexa Fluor 647 coupled anti-rabbit or anti-mouse secondary antibodies (Invitrogen); the respective number of foci analysed are stated in Fig. 1. To verify mitochondrial localization of the analysed foci, we co-stained the mitochondrial proteins TOMM20 or mtHSP70 using the respective primary antibodies and Alexa Fluor 488 coupled secondary antibody (Invitrogen). For two-colour htSTORM, we used Alexa Fluor 647 for BrU coupled with DyLight 755 (Invitrogen) to label FASTKD2 and we analysed 12 FOVs from four distinct imaging days. To allow lateral drift-correction, 100-nm gold nanospheres coated with poly-L-lysine were incubated on each sample for 5 min before the sample was mounted on the microscope with fresh imaging buffer. Before acquiring each raw STORM stack (10-ms exposure, 20,000–40,000 frames), we collected a 50-ms wide-field reference image at low laser power. Manually incrementing the 405 nm activation laser power allowed prolonged imaging. Imaging conditions (excitation illumination powers of 500–1,500 mW) were adjusted according to sample type.

We analysed and plotted the obtained localizations by adapting published MATLAB³⁹ and new Python scripts (Supplementary Fig. 1). In brief, adaptations of data processing encompassed manual selection of regions of interest (ROIs) around MRGs that were in focus. For two-colour experiments, this selection was applied very restrictively, verifying the presence of a bright wide-field signal in both channels. For two-colour experiments, additional care was paid to reduce effects due to chromatic aberrations. For this, the localizations of every selected ROI were visually inspected, and ROIs were rejected from further analysis unless no visually detectable systematic shift was visible following DBSCAN clustering³⁸.

All descriptors were computed from localizations belonging to each particular cluster. We calculated the FWHM from the summed eigenvalues as the diameter for each granule using a Python script provided here. The eccentricity was determined as the ratio between the long axis and the short axis. Axis lengths are the eigenvalues of the covariance matrix of clustered localizations in the *x* and *y* dimension as described in ref. 40. We used the MATLAB function 'convexHull' to compute granule area and identify the hull-defining edge points. Three data points >0.25 µm² were omitted for the creation of Supplementary Fig. 1, but kept for all statistical analysis. The radius of gyration was computed as the sum of variances in *x* and *y*, divided by the number of localizations. Sigma was computed as the sum of the eigenvalues in *x* and *y*.

SIM live-cell microscopy. SIM was performed on a three-dimensional (3D) NSIM Nikon microscope with a CFI Apochromat TIRF objective (×100, numerical aperture (NA) 1.49, Nikon). The microscope was equipped with 400-mW, 561-nm and 480-mW, 488-nm lasers (Coherent Sapphire) and a back-illuminated electron-multiplying charge-coupled device camera (iXon 3, Andor Technology). Live-cell imaging was performed at 37°C, using 488- and 561-nm lasers for eGFP and tRFP excitation, respectively. Imaging settings were adapted to yield the best image quality with minimal photobleaching at a laser power between 2 and 10% and 3–10 s per frame. Per field of view, 15 raw images were acquired in 3D-SIM imaging mode to ensure the highest signal-to-noise ratio and resolution. Final, super-resolved SIM images were reconstructed using the commercial Nikon NIS-Elements software (v. 3.2.2) and analysed in Fiji (ImageJ 2.0.0-rc-69/1.52p). Open-source MicrobeJ software⁴¹, originally developed for analysis of bacteria, was used for supervised automatic segmentation of mitochondria and location of their associated foci (Supplementary Fig. 4).

FRAP and confocal microscopy. For FRAP assays, cells were seeded on coverslips and grown to 60–80% confluence. Coverslips were mounted on a Zeiss LSM 700 inverted confocal microscope with a Plan-Apochromat oil objective (×63, NA 1.40). Microscope acquisitions were controlled by the Zen (2009 v. 6.0.0) software from Zeiss. The microscope was equipped with 488-nm and 555-nm solid-state lasers and three photomultipliers for simultaneous transmission and epifluorescence recording. A sliding prism and green and red bandpass filters were used to ensure clean fluorescence emission. For live assays, an Okolab stage top incubator H301 was used to maintain the sample temperature at 37°C. Cells were maintained in CO₂-independent Leibovitz L-15 medium (Gibco). For FASTKD2- (*n*_{eGFP} = 44, *n*_{tRFP} = 31, *n*_{tRFP-Drp1KD} = 40), ERAL1- (*n* = 17) and DDX28- (*n* = 16) FRAP, the pixel size was reduced to 70 nm (zoom = 12) and line scans were recorded at a pixel dwell time of 2.55 µs (maximum speed), resulting in a scan time of 97.75 ms per 128 × 128-pixel FOV. The pinhole was opened for FRAP recording. The 10 × 10-pixel ROIs were manually drawn around single MRGs for FRAP and two or three pre-bleach time points were acquired for normalization. FASTKD2-eGFP in COS-7- (*n* = 75) and U2OS- (*n* = 38), and TWINKLE-eGFP (*n* = 50) FRAP were acquired with twice as many pixels (254 × 254 and 20 × 20 ROI) but for the same sample region (zoom = 12). A different FOV was chosen for every FRAP experiment and multiple different cells could be imaged per sample, but samples

were exchanged after ~1 h of imaging and when low mitochondrial motility was noticeable, to avoid confounding effects of deteriorating cell health. If MRGs had left the ROI before bleaching, the assay was aborted and a different MRG was chosen. Recovery was monitored over 50–60 s at 1 f.p.s.

For confocal microscopy of fixed cells, samples were prepared as described above. Alexa Fluor 488, 594 or 647 secondary conjugated antibodies (Invitrogen) were used to visualize the immunolabelled targets. Imaging was performed using a Leica TCS SP8 inverted microscope with a Plan-Apochromat oil objective ($\times 63$, NA 1.4), using the Lightning mode (Leica) to generate deconvolved images. Microscope acquisitions were controlled by LAS X (v. 3.5.2) software from Leica. The microscope was equipped with 405-, 488-, 552- and 638-nm lasers. Imaging for Extended Data Fig. 7 was performed using a Molecular Devices ImageXpress Micro XL automated wide-field microscope, equipped with an air objective ($\times 60$).

FRAP analysis and software. For FRAP recording of moving objects, a custom Fiji script was co-developed with O. Burri from the Bioimaging and Optics Platform (BIOP) at EPFL. In brief, this script, ‘TrackFRAP’, is based on the Fiji plugin TrackMate and automatically follows the bleaching ROI during recovery. It allows the user to choose other foci as FRAP references for overall bleaching correction and outputs both a list of intensity values and metadata to allow reproducible data analysis. All tracks were manually inspected to ensure the bleached granule was recorded correctly over the full course of acquisition. If no reference granule could be tracked over the full acquisition period, the dataset was excluded from analysis. We then developed a Python script to load and analyse TrackFRAP data, which we termed FRAPtrackAnalyser (FRAPtA) and which is based on the FRAPAnalyser tool⁴². Single or double exponentials were fit and plotted for each dataset, as well as used to extract recovery times.

Correlative confocal light and electron microscopy. Cells were seeded on a gridded coverslip (MatTek, P35-1.5-14-CGRD-D), transfected with CFP-Drp1 (K38A) plasmid if applicable, and grown to 50–60% confluence. Cells were then fixed at room temperature for 1 h in fresh fixative (2% PFA, 1% glutaraldehyde in PBS 0.1 M pH 7.4), washed in PBS and imaged by confocal microscopy the same day. Z-stacks were acquired of whole cells, with the pinhole closed to 0.5 Airy units (AU) and the pixel size reduced to 50–100 nm in the *x*-*y* dimensions and 100–150 nm in the *z* dimension. Samples were then stored overnight in PBS, at 4 °C. They were then stained with osmium and potassium ferrocyanide, followed by osmium alone, each with cacodylate buffer. They were finally stained with 1% uranyl acetate, then washed in water, dehydrated with increasing concentrations of alcohol, and infiltrated with EPON resin. This was polymerized overnight at 65 °C. Serial, ultra-thin sections were then cut of the cell of interest and the sections were collected on single-slot copper grids with a formvar support membrane. Images were recorded in a transmission electron microscope operating at 80 kV (FEI Company, Tecnai Spirit).

Mitochondrial sub-fractionation and western blotting. To perform mitochondrial sub-fractionation experiments, HeLa cells were grown to ~60% confluency in four 150-mm Petri dishes. Cells were washed in PBS and collected by mechanical scraping. For a first mitochondrial extraction, cells were broken in cold mannitol buffer (MB) (210 mM mannitol, 70 mM sucrose, 10 mM HEPES-KOH pH 7.4, 1 mM EDTA) in the presence of protease inhibitors (Roche), using a syringe with a G25 n18 needle. Cell passage through the needle was repeated 20 times. Unbroken cells and nuclei were discarded in the pellet after centrifugation for 5 min at 1,000g at 4 °C, followed by a second centrifugation for 5 min at 2,500g at 4 °C. The mitochondria-rich fraction was pelleted by centrifugation for 10 min at 6,000g at 4 °C, then the pellet was washed in 1 ml of fresh MB buffer and centrifuged again for 15 min at 13,000g at 4 °C.

To further proceed with sub-mitochondrial fractionation and remove the OMM, mitoplasts were prepared by gently resuspending the mitochondria in cold 10 mM HEPES buffer pH 7.4 in the presence of protease inhibitors (Roche) and 1 U μl^{-1} of RNAsin (Promega), at a final concentration of 0.5 μg of mitochondria per μl . After incubation for 20 min on ice, mitoplasts were recovered in the pellet by centrifugation for 15 min at 15,000g at 4 °C. Finally, to obtain the IMM and matrix fractions, mitoplasts were resuspended in MB buffer (in the presence of protease and RNase inhibitors) and sonicated using a water bath sonicator Bioruptor TM Twin with 30-s pulses for 15 cycles at 4 °C. After sonication, the samples were ultra-centrifuged for 30 min at 45,000g at 4 °C, to obtain a pellet corresponding to the IMM-rich fraction and a supernatant corresponding to the matrix-rich fraction. Mitochondria-, IMM- and matrix-rich fractions were analysed by SDS-PAGE using 4–20% gradient Novex TM Tris-glycine gels (Thermo Fisher Scientific).

For immunoblotting, proteins were transferred electrophoretically to PVDF membranes (GE Healthcare) and exposed to the primary antibodies listed below, diluted in 5% non-fat dry milk in Tris buffered saline with Tween 20 (TBST). The blots were further incubated with anti-mouse or anti-rabbit horseradish peroxidase-conjugated secondary antibodies (Dako, P0447 and P0448 respectively; used at 1:5,000–1:10,000 dilution), and visualized using an ECL system (GE Healthcare). Where required, images of western blots were treated for contrast enhancement and band intensities were quantified using ImageJ.

Primary antibodies used for western blots. The primary antibodies used for western blots were anti-FASTKD2 (Proteintech, 17464-1-AP), anti-GRSF1 (Sigma, HPA036985), anti-FASTKD5 (Sigma, SAB2700438), anti-TFAM (Proteintech, 22386-1-AP), anti-mtSSB (Proteintech, 12212-1-AP), anti-PHB (Thermo Fisher Scientific, MS-261-PO), anti-OxPhos Complex IV subunit IV (clone 20E8C12, Thermo Fisher Scientific, A21348) and anti-PDHE1 α (GeneTex, GTX104015). All primary antibodies were diluted 1:2,000.

Stimulated emission depletion microscopy. STED microscopy was performed on a Leica TCS SP8 STED 3X inverted microscope equipped with an HC PL-APO glycerol motC STED W objective ($\times 93$, NA 1.30) for fixed samples or an HC PL-APO oil objective ($\times 100$, NA 1.40) for live samples. The microscope was equipped with a white light laser (470–670 nm) and 592-nm and 775-nm (pulsed) depletion lasers for STED.

For fixed-cell STED microscopy, samples were prepared following the immunofluorescence protocol described above. Abberior STAR 580 and Abberior STAR RED secondary antibodies (Abberior) were used in combination to label the primary antibodies. Coverslips were mounted on slides using Prolong Gold Antifade mounting agent (Thermo Fisher Scientific). STED depletion lasers were set to 70% of maximum power. The pinhole was opened to 1 AU for image acquisition. The LIGHTNING mode (Leica) was used to deconvolve STED images.

For live-cell STED microscopy, we followed the sample preparation and adapted the imaging protocol as recently published in ref.³¹. In brief, HeLa Cox8a-SNAP cells were seeded onto coverslips the day before imaging. Following antimycin A treatment, cells were incubated at 37 °C for 15–30 min with 1 μM SNAP-Cell SiR fluorescent substrate (New England Biolabs), followed by a 15–30-min washing step in dye-free medium. Cells were imaged at 37 °C in Life cell imaging solution (Thermo Fisher Scientific). For live-cell STED acquisitions, the pinhole was set to 1 AU, the zoom was set to $\times 5$ –9 and the pixel size automatically adapted. The SiR was excited at 640 nm with 775-nm depletion at 60–70%. Fine-tuning the gating (1–5 ns) and emission-filter bandwidths proved vital. Dwell times were around 8 μs , and 8 \times line-accumulation was used to obtain the best images. The FASTKD2-eGFP signal to visualize the MRGs was acquired in confocal mode and each line was scanned once. No deconvolution was used. The presented images are raw data, adjusted for brightness and contrast using Fiji software.

Statistics and reproducibility. All plotting and statistical analysis was performed using Python 3, with Jupyter Notebook 6.0 used to document analyses. Mann–Whitney U, Students *t* and Kolmogorov–Smirnov tests were used as indicated, and computed using the Python scipy-library, seaborn- and matplotlib-libraries were used to plot the figures, and to add statistical significance indicators we used the statannot-library⁴³. To avoid conflicts with non-Gaussian distributions we report the median values, unless stated otherwise. Correlation coefficients are calculated as Pearson’s *R* using numpy-library. Analysis is reproducible through automated analysis scripts.

Reporting Summary. Further information on research design is available in the Nature Research Reporting Summary linked to this article.

Data availability

All imaging as well as numerical data relevant to this study are publicly available in the online repository Zenodo (<https://doi.org/10.5281/zenodo.3747143>) or upon reasonable request. A README-file on Zenodo will guide the reader. All remaining other data supporting the findings of this study are available from the corresponding author on reasonable request. Plasmids and cell lines are available; please contact the corresponding authors. Source data are provided with this paper.

Code availability

All code including adapted STORM-analysis code, TrackFRAP, FRAPtA and other python scripts and Fiji macros for analysis and figure generation are available in the online repository GitHub (<https://github.com/TimoHenry/MitochondrialRNAgranules>), or upon reasonable request. Jupyter Notebooks are available in the data repository on Zenodo to trace the application of the code to the data in our manuscript.

References

- Sieben, C., Banterle, N., Douglass, K. M., Gonczy, P. & Manley, S. Multicolor single-particle reconstruction of protein complexes. *Nat. Methods* **15**, 777–780 (2018).
- Spruyt, V. A *Geometric Interpretation of the Covariance Matrix* (Computer Vision for Dummies, 2014); <https://www.visiondummy.com/2014/04/geometric-interpretation-covariance-matrix/>
- Ducret, A., Quardokus, E. M. & Brun, Y. V. MicrobeJ, a tool for high throughput bacterial cell detection and quantitative analysis. *Nat. Microbiol.* **1**, 16077 (2016).

42. Halavatyi, A., Yotskou, M. & Friederich, E. FRAPAnalyser (OMICtools, 2008); <https://omictools.com/frapanalyser-tool>
43. Weber, M. 'statannot' (GitHub, 2019); <https://github.com/webermarcolivier/statannot>

Acknowledgements

We thank H. Perreten for molecular cloning, F. Prodon for help with STED microscopy, O. Burri for the initial FRAPtrack code and the BIOP (EPFL) for imaging support. We thank R. Jajoo for his generous sharing of original code and data, and T. Stephan and S. Jakobs for the unreserved provision of Cox8a-SNAP cell lines and plasmids. We also thank M. Colomer and M. Martinez for their contribution to assessing MRG distribution. We are grateful to C. Sieben, K. Douglass, T. Kleele, J. Griffié and all members of the Manley and Martinou groups for discussions. Flow cytometry cell sorting was performed at the EPFL Flow Cytometry Core Facility. Electron microscopy was performed at the EPFL BioEM facility. Fluorescence microscopy was partially performed at the EPFL Bio Optics Platform (BIOP) and the UniGe Bio Imaging Core facility. This work was supported by the European Research Council (ERC CoG 819823, Piko to S.M. and T.R.) and the Swiss National Science Foundation (31003A_179421 to J.-C.M.).

Author contributions

S.Z., T.R., J.-C.M. and S.M. conceived and designed the study and wrote the manuscript. All authors reviewed and edited the manuscript. T.R. and S.Z. designed, executed, analysed and validated the experiments. E.C. executed and coded FRAP experiments and analysis. E.V. performed fractionation and western blotting. M.C. embedded, sectioned and acquired transmission electron microscopy samples. T.R. and S.Z. prepared the figures and plots. S.M. and J.-C.M. supervised the project.

Competing interests

The authors declare no competing interests.

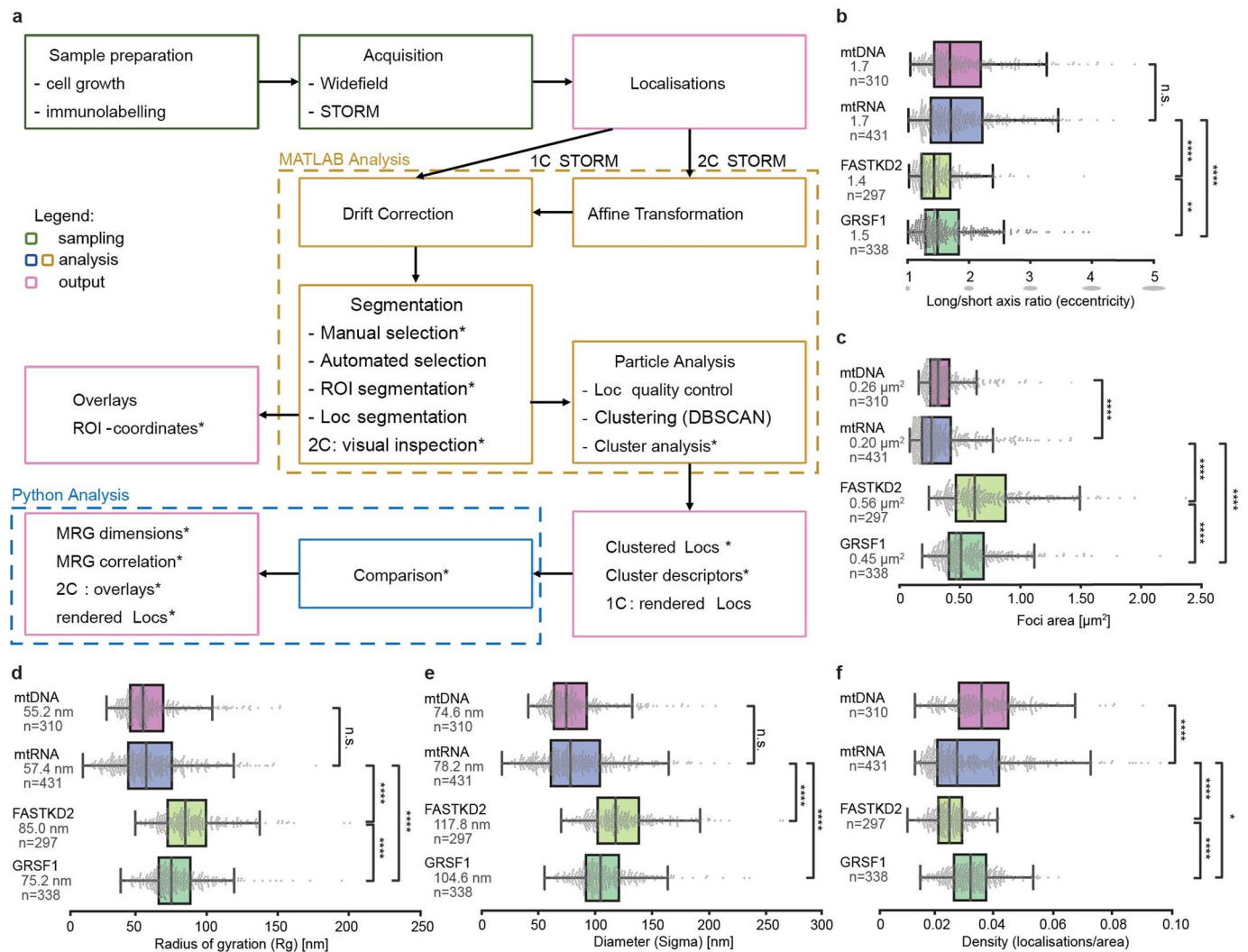
Additional information

Extended data is available for this paper at <https://doi.org/10.1038/s41556-020-00584-8>.

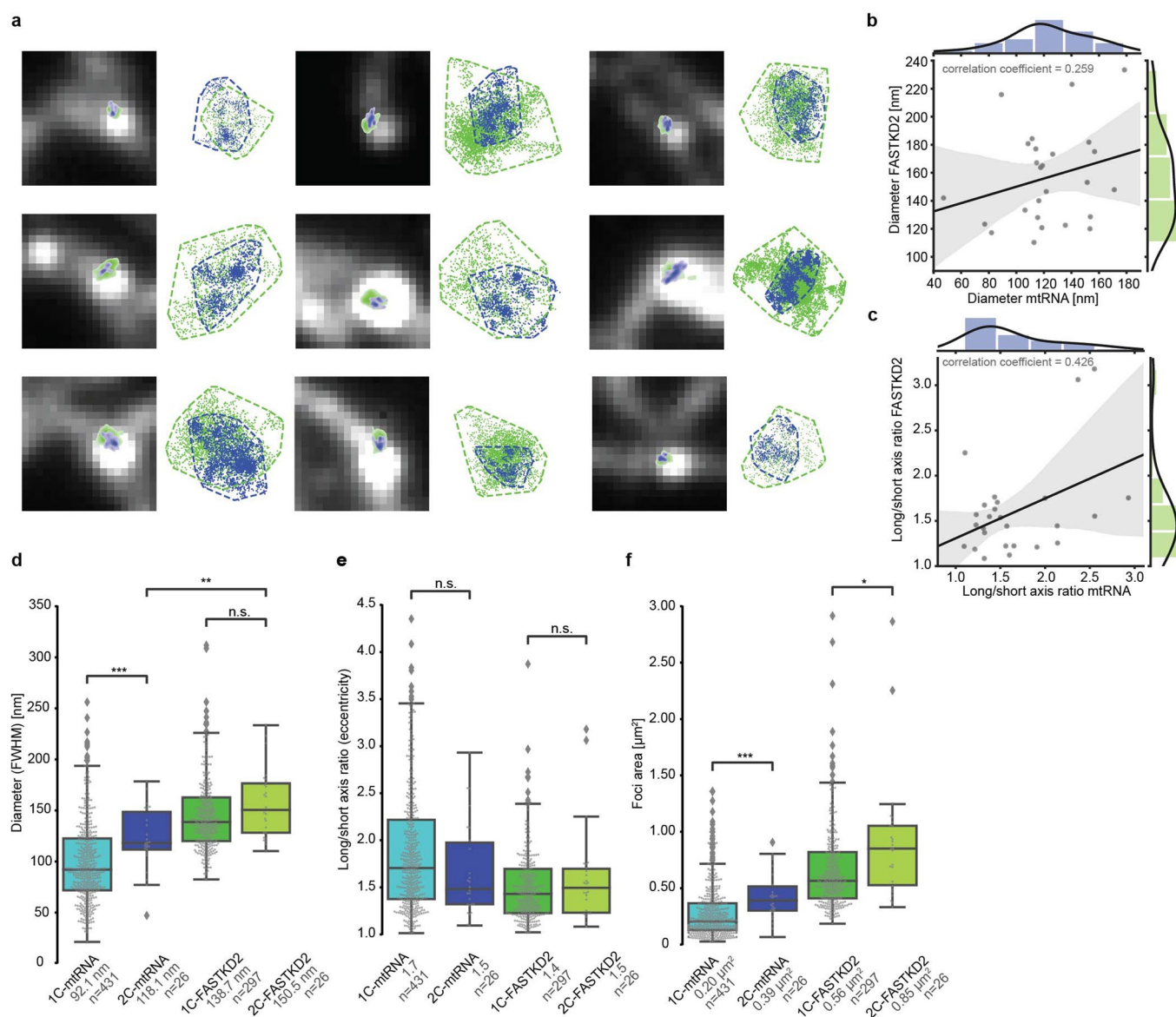
Supplementary information is available for this paper at <https://doi.org/10.1038/s41556-020-00584-8>.

Correspondence and requests for materials should be addressed to T.R., J.-C.M. or S.M.

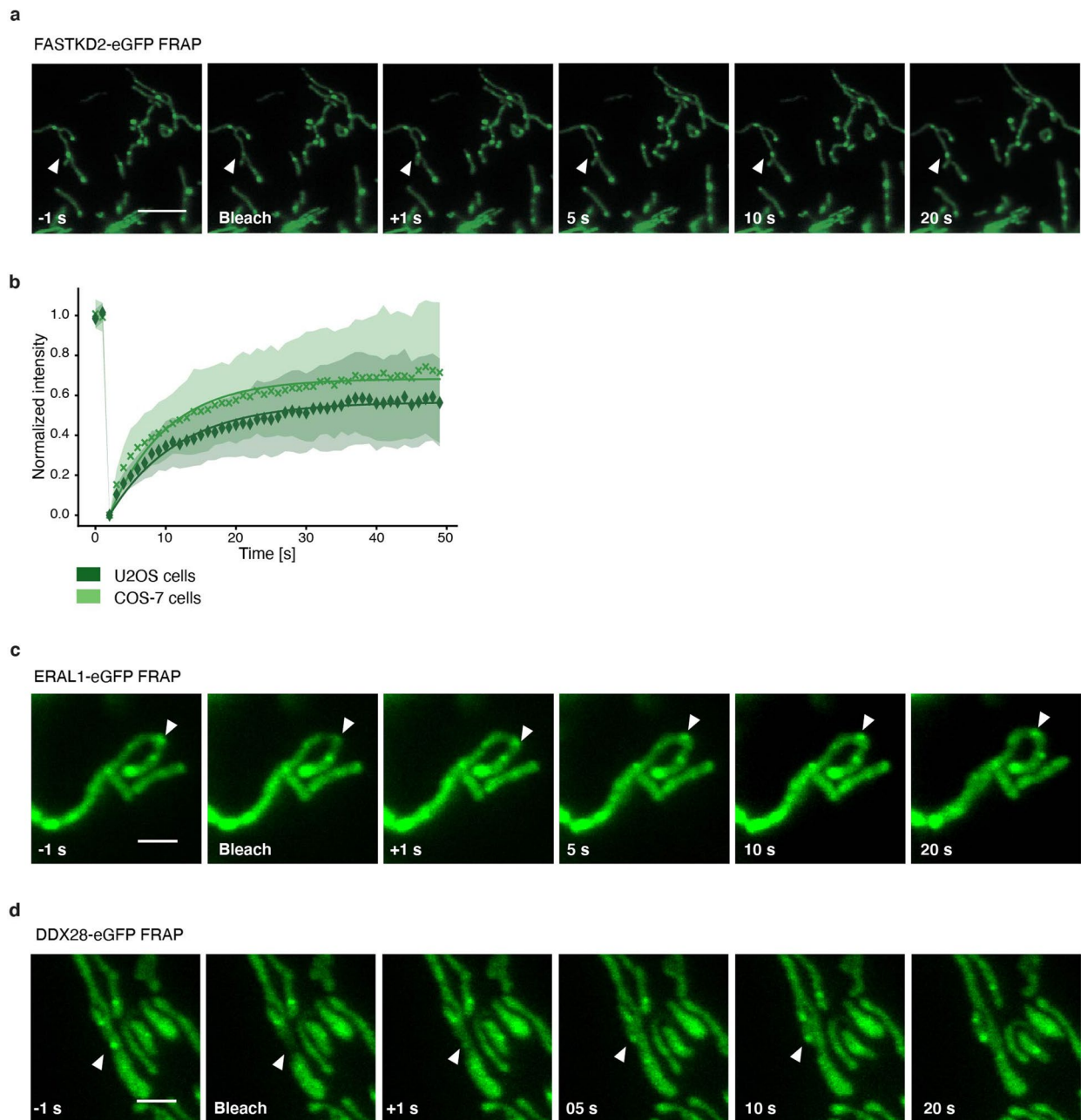
Reprints and permissions information is available at www.nature.com/reprints.



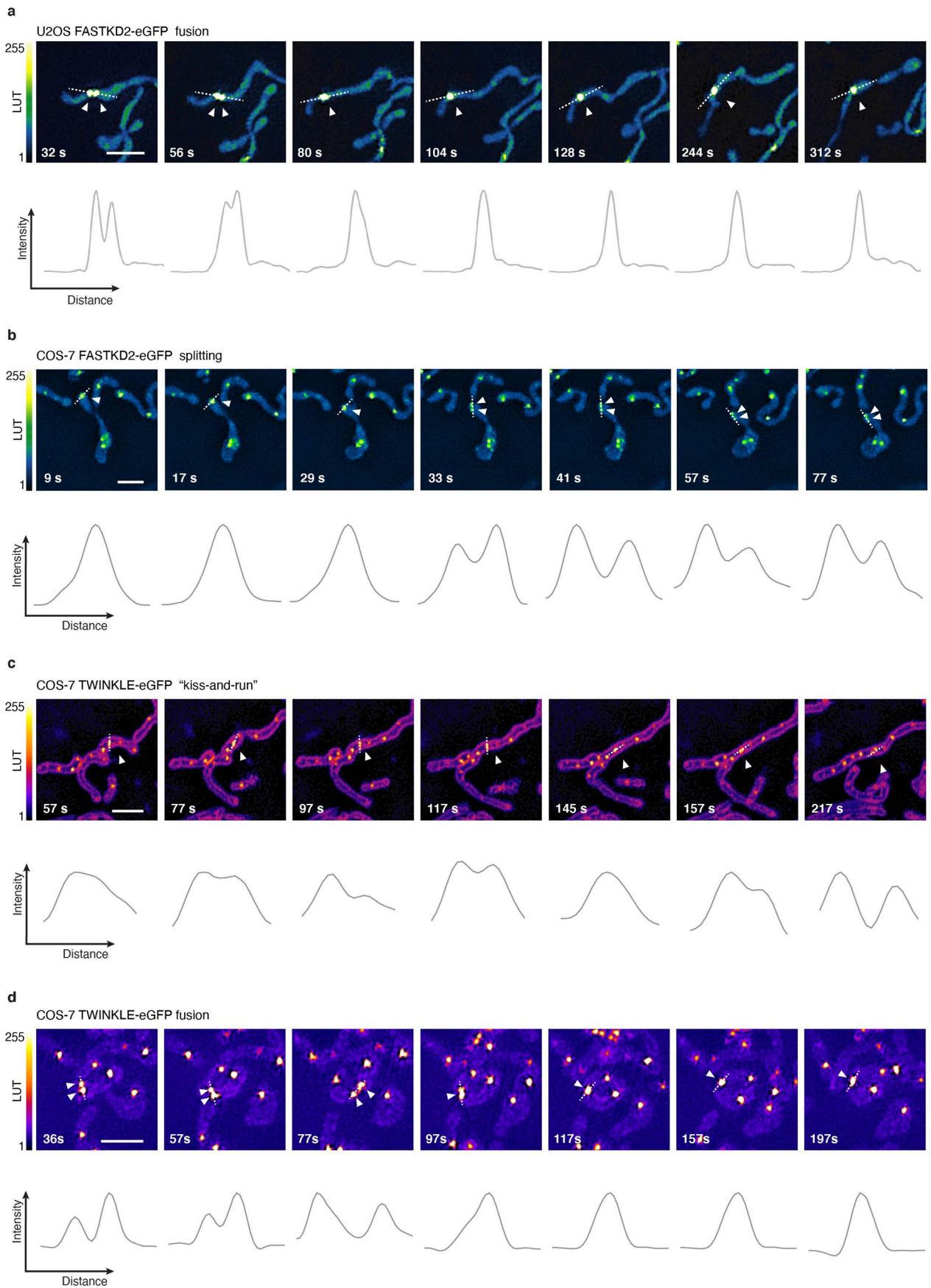
Extended Data Fig. 1 | Workflow and quantification of nanoscopic architecture of MRGs. a, Workflow used for this study. Previously unpublished parts of the analysis are highlighted by asterisks, while other parts were previously published¹⁷³⁶. **b-f** Additional quantification of MRG and nucleoid (mtDNA) architecture from htSTORM data. Markers (mtRNA, FASTKD2 and GRSF1), number of granules n and median values are indicated for each condition; n.s. denotes p -values > 0.05 , * denotes p -values ≤ 0.05 , ** denote p -values ≤ 0.01 , *** denote p -values ≤ 0.001 , **** denote p -values ≤ 0.0001 of two-sided Mann-Whitney-U test. Individual data points are plotted grey, box plots denote first and third quartiles, and the median, whiskers comprise rest of distributions except outliers. Multiple acquisitions, samples and imaging days were pooled. **b**, Median eccentricity of both MRG-proteins differ slightly ($p = 5.1e^{-3}$), with largely overlapping boxes and can be approximated by spheres. Nucleoids and nascent RNA components of MRGs are more elongated ($p_{\text{BrU-FASTKD2}} = 1.4e^{-15}$, $p_{\text{BrU-GRSF1}} = 1.7e^{-6}$). **c**, Comparison of areas described by convex hull. MRG-protein foci are significantly larger than nascent-RNA foci ($p_{\text{BrU-FASTKD2}} = 2.7 \times 10^{-61}$, $p_{\text{BrU-GRSF1}} = 6.5 \times 10^{-49}$), yet less different from one another ($p_{\text{GRSF1-FASTKD2}} = 6.9 \times 10^{-7}$). The distribution of mtRNA- and mtDNA-foci areas strongly overlap, though their medians are significantly different with $p_{\text{mtRNA-mtDNA}} = 1.2 \times 10^{-6}$. Three outliers for FASTKD2 ($> 2.5 \mu\text{m}^2$) were removed for better visualisation, but included in all quantitative analysis. **d**, and **e**, Comparison of alternative standard point-cloud descriptors Radius of gyration (R_g), and Sigma as the average of the eigenvalues in two dimensions, and multiplied by two to yield a diameter. **f**, Density of localisations was also compared, and both GRSF1 and FASTKD2-foci follow a narrow normal distribution, while mtDNA & BrU show a larger variance of density. Number (n) of clusters quantified for each condition is represented in the figure and is pooled from 24, 13, 7, and 14 FOVs, and 4, 4, 3, and 2 samples for BrU, GRSF1, FASTKD2, and mtDNA respectively. Statistical source data are provided in Source data Extended data Fig. 1.



Extended Data Fig. 2 | Comparison and correlation of two-colour htSTORM data. **a**, Nine additional examples of two-colour htSTORM of MRGs. Scatter plots of localisations (right) are shown next to corresponding clusters of FASTKD2 (green) and mtRNA (BrU, blue) overlaid on widefield images (left). Convex hull areas are represented with dashed lines. **b**, and **c**, Scatter plots of all FASTKD2-mtRNA (BrU) pairs with regression-fit (black) and standard deviation (grey). Histograms of the distribution for FASTKD2 (y-axis, right, green), and mtRNA (x-axis, top, blue), including a kernel density estimate are shown. No correlation of Diameter (FWHM) ($R = 0.26$) or eccentricity (length/width, $R = 0.43$) was found between FASTKD2 and BrU foci from individual granules ($n=26$ MRGs over 4 independent experiments). **d-f**, Comparison of foci characteristics for one- versus two-colour htSTORM by Two-sided Mann-Whitney-U test from two-colour to one-colour data. Number of granules n (pooled from 20 FOVs, and 8 samples) and median values are indicated for each condition; n.s. denotes p -values > 0.05 , * denotes p -values ≤ 0.05 , ** denote p -values ≤ 0.01 , *** denote p -values ≤ 0.001 , **** denote p -values ≤ 0.0001 . **d**, FWHM is not significant for FASTKD2 ($p = 0.22$) but two-colour BrU foci were significantly larger ($p = 8.8e^{-4}$), and two-colour FASTKD2 were also larger than two-colour-mtRNA ($p = 0.0014$). **e**, Eccentricity is not significantly different ($p_{\text{mtRNA}} = 0.36$, $p_{\text{FASTKD2}} = 1.0$). **f**, Size determined by convex hull, differed between one-colour and two-colour BrU ($p = 2.4e^{-4}$) as well as FASTKD2 ($p = 0.017$). This may in parts be due to the heavy weight of two outliers as visible in the plot. Statistical source data are provided in Source data Extended data Fig. 2.

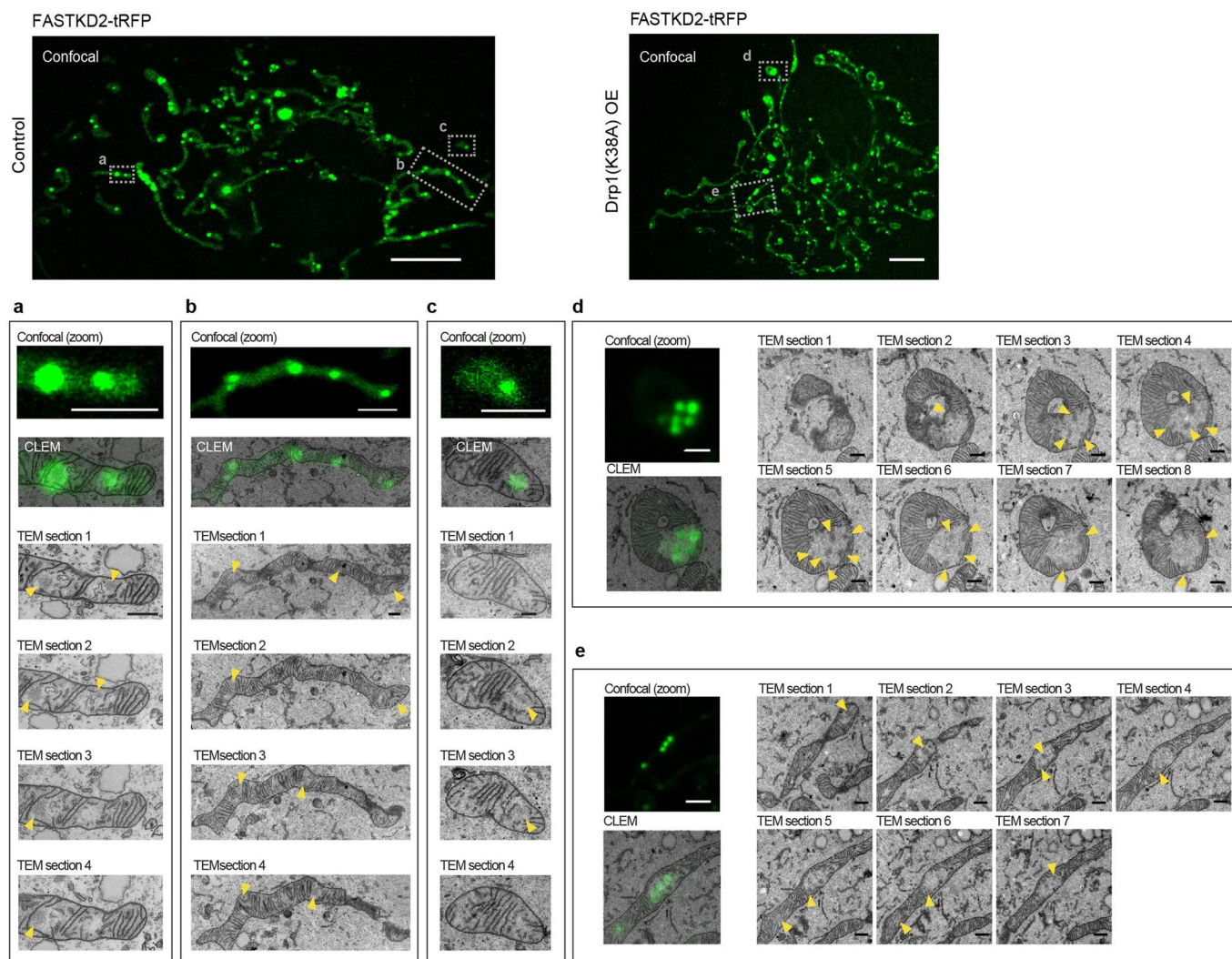


Extended Data Fig. 3 | FRAP of MRG-associated proteins. **a**, Representative time-lapse images of MRGs FRAP experiments in U2OS cells stably expressing FASTKD2-eGFP (green) ($n = 39$ MRGs examined over 3 independent experiments). White arrowheads indicate the photobleached structures. Scale bar: $5 \mu\text{m}$. **b**, FRAP analysis of FASTKD2-eGFP in U2OS ($n = 39$ MRGs examined over 3 independent experiments) and COS-7 cells ($n = 44$ MRGs examined over 8 independent experiments). Symbols in the graph represent mean data points. Single exponential fits (lines) and standard deviations for each time point (shaded area) are shown. **c**, **d**, Representative time-lapse images of ERAL1- ($n = 17$ MRGs examined over 3 independent experiments) and DDX28-eGFP ($n = 17$ MRGs examined over 3 independent experiments) FRAP experiments in COS-7 cells. White arrowheads indicate the photobleached structures. These images correspond to the data plotted in Fig. 2c. Scale bar: $2 \mu\text{m}$.

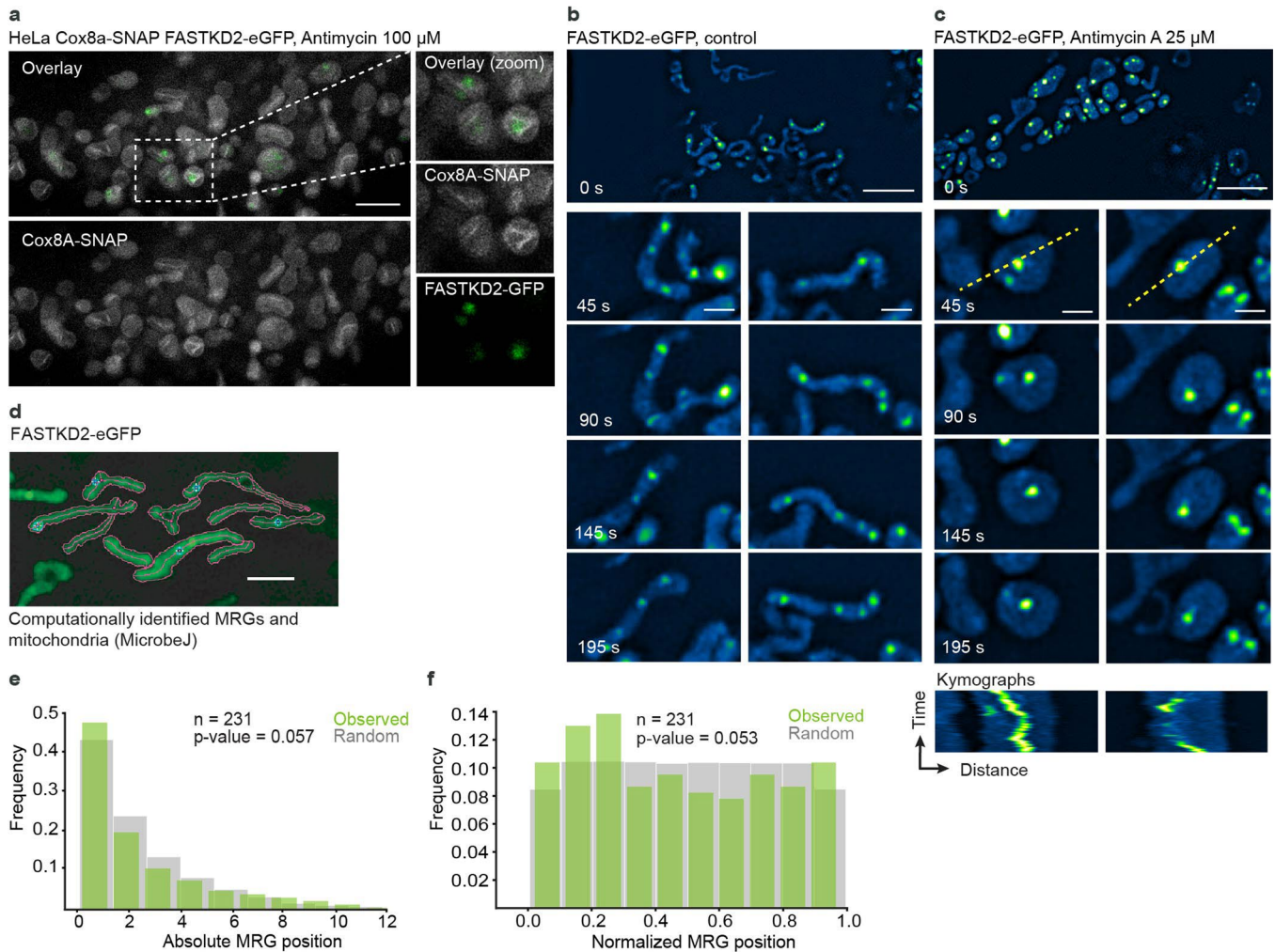


Extended Data Fig. 4 | See next page for caption.

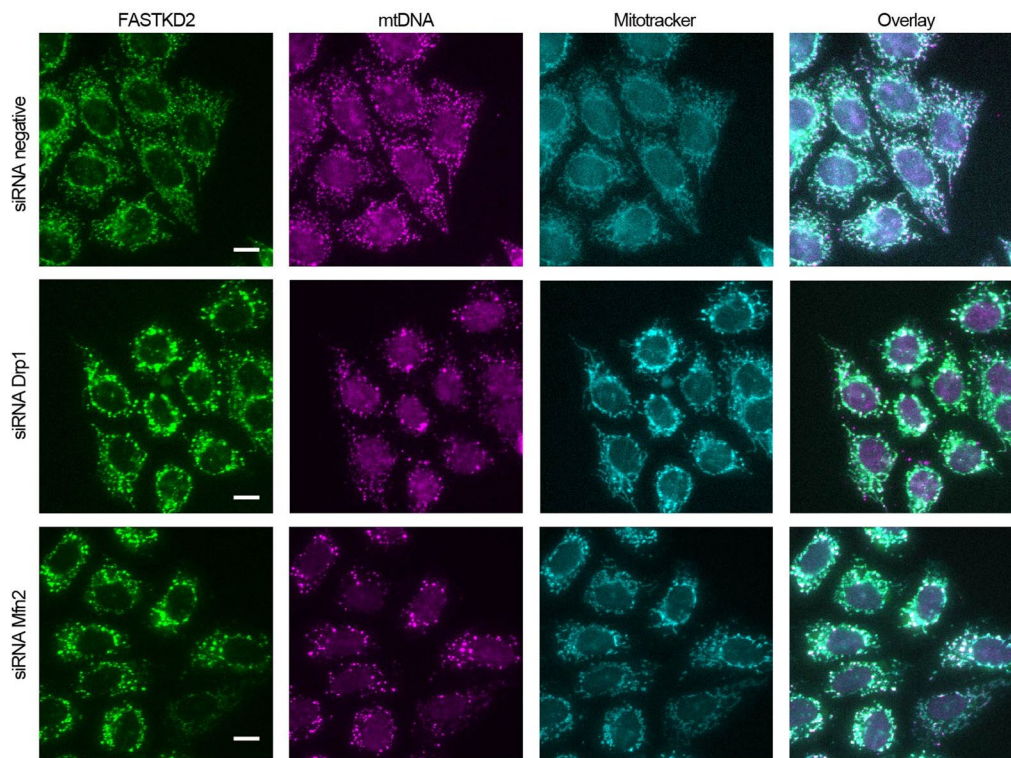
Extended Data Fig. 4 | MRG and nucleoid dynamics in live cells. **a**, Representative time-lapse images of an MRG fusion event in a live U2OS cell, monitored by SIM. MRGs are visualized by stable expression of FASTKD2-eGFP (n= 7 cells). **b**, Representative time-lapse images of an MRG splitting event in a live COS-7 cell, monitored by SIM. MRGs are visualized by stable expression of FASTKD2-eGFP (n= 6 cells). **c, d**, Representative time-lapse images of nucleoid “kiss-and-run” (n=1 cell) and splitting events (n=2 cells), respectively, in COS-7 cells, monitored by SIM. Nucleoids are visualized by transient expression of TWINKLE-eGFP and mitochondrial outlines are highlighted by TOMM20-eGFP expression. **a-d**, Cells were imaged at 1/5 Hz. White arrowheads indicate the dynamic events. Dashed lines indicate the segments used to measure the intensity (grey values) represented in the plots below. Linear Fire LUTs are used to represent pixel intensity values. Scale bars: 2 μm . Statistical source data are provided in Source data Extended data Fig. 4.



Extended Data Fig. 5 | CLEM of FASTKD2-tRFP and MRG electron densities. Correlative confocal fluorescence micrograph of FASTKD2-tRFP and transmission electron micrograph (TEM) in COS-7 control (**a - c**) (7 MRGs were examined from 3 mitochondria of a single cell) and Drip1^{K38A}-CFP positive (**d, e**) (10 MRGs were examined from 2 mitochondria of a single cell) cells. TEM-highlights correspond to the data presented in Figs. 3a and 4e respectively, and show additional examples. Contiguous 50 nm TEM microtome sections show electron densities corresponding to the MRGs visualized by fluorescence microscopy (yellow arrowheads). Scale bars: Confocal: 10 μ m; Confocal zoom: 2 μ m; CLEM and TEM sections: 500 nm.



Extended Data Fig. 6 | Membrane association and distribution of MRGs within mitochondria. **a**, STED microscopy of HeLa cells stably expressing Cox8a-SNAP (grey) and FASTKD2-eGFP (green), treated with 100 μ M antimycin A for 1 hour, prior to labelling with SIR-SNAP dye and live cell imaging (The experiment has been performed twice with similar results). A zoomed field of view on the right (dashed box). Scale bar: 2 μ m. **b-c**, FASTKD2-eGFP expressing COS-7 cells untreated (**b**) or treated with 25 μ M antimycin A for 24 hours (**c**), imaged live using SIM microscopy. The same linear Fire LUT is used for pixel intensity values as in Fig. 2e. Zoomed time-lapse series are shown for two mitochondria (dashed boxes) (The experiment has been performed twice with similar results). Kymographs below (plotted lines are represented on the analysed mitochondria as yellow dashed lines). Scale-bar: 2 μ m. **d**, Example FOV of semi-automated mitochondria segmentation and MRG-association with their parent organelle with the ImageJ plugin, MicrobeJ. (The experiment has been performed three times with similar results). **e**, and **f**, Histograms of absolute or relative position of MRGs (n = 231 MRGs examined over 3 independent experiments) within their host mitochondria (green) and simulated, randomly positioned granules (grey). The observed distribution of MRG positions is not significantly different from the simulated random distribution (Kolmogorov-Smirnov test: $p_{\text{abs}} = 0.057$, $p_{\text{norm}} = 0.053$). Statistical source data are provided in Source data Extended data fig. 6.



Extended Data Fig. 7 | Effect of perturbations to mitochondrial dynamics on MRG distribution. Representative widefield-microscopy images of HeLa cells silenced using siRNAs against Drp1 (second row) or Mfn2 (third row). Cells were fixed after 72 hours of silencing. A negative control siRNA was used in parallel, and is shown in the first row. MRGs and nucleoids were immunolabeled using anti-FASTKD2 (green) and anti-DNA (magenta), respectively. Mitochondria were labelled using MitoTracker Deep Red staining (cyan) (The experiment has been performed twice with similar results). Scale-bar: 10 μm . Disrupted MRG and nucleoid positioning, and clumped appearance as described for mito-bulbs is apparent when either Drp1 and Mfn2 are silenced, but the negative control shows well-dispersed MRGs and nucleoids.

Reporting Summary

Nature Research wishes to improve the reproducibility of the work that we publish. This form provides structure for consistency and transparency in reporting. For further information on Nature Research policies, see [Authors & Referees](#) and the [Editorial Policy Checklist](#).

Statistics

For all statistical analyses, confirm that the following items are present in the figure legend, table legend, main text, or Methods section.

n/a Confirmed

- The exact sample size (n) for each experimental group/condition, given as a discrete number and unit of measurement
- A statement on whether measurements were taken from distinct samples or whether the same sample was measured repeatedly
- The statistical test(s) used AND whether they are one- or two-sided
Only common tests should be described solely by name; describe more complex techniques in the Methods section.
- A description of all covariates tested
- A description of any assumptions or corrections, such as tests of normality and adjustment for multiple comparisons
- A full description of the statistical parameters including central tendency (e.g. means) or other basic estimates (e.g. regression coefficient) AND variation (e.g. standard deviation) or associated estimates of uncertainty (e.g. confidence intervals)
- For null hypothesis testing, the test statistic (e.g. F , t , r) with confidence intervals, effect sizes, degrees of freedom and P value noted
Give P values as exact values whenever suitable.
- For Bayesian analysis, information on the choice of priors and Markov chain Monte Carlo settings
- For hierarchical and complex designs, identification of the appropriate level for tests and full reporting of outcomes
- Estimates of effect sizes (e.g. Cohen's d , Pearson's r), indicating how they were calculated

Our web collection on [statistics for biologists](#) contains articles on many of the points above.

Software and code

Policy information about [availability of computer code](#)

Data collection

STORM: Micromanager 2.0 beta & APT Software (v. 3.21.4). Localization with MATLAB 2016b for Windows 10.
FRAP: ZEN 2009.
SIM: NIS-Elements (v. 3.2.2)
Confocal: Zeiss ZEN (v 6.0.0)
STED: LAS X (v. 3.5.2). With LIGHTNING deconvolution

Data analysis

STORM: DBSCAN MATLAB function; customized MATLAB script; MATLAB 2018a, Anaconda 3 & jupyter notebooks (Python3).
FRAP: customized Fiji script: TrackFRAP, available on GitHub; ImageJ 2.0.0.-rc-69/1.52p & Python3.
SIM: MicrobeJ (v. 5.131 (20) - beta; ImageJ plugin), Python3
CLEM: Fiji (ImageJ 2.0.0.-rc-69/1.52p)
all customized software will be made publicly available. Link: <https://github.com/TimoHenry/MitochondrialRNAgranules>

For manuscripts utilizing custom algorithms or software that are central to the research but not yet described in published literature, software must be made available to editors/reviewers. We strongly encourage code deposition in a community repository (e.g. GitHub). See the Nature Research [guidelines for submitting code & software](#) for further information.

Data

Policy information about [availability of data](#)

All manuscripts must include a [data availability statement](#). This statement should provide the following information, where applicable:

- Accession codes, unique identifiers, or web links for publicly available datasets
- A list of figures that have associated raw data
- A description of any restrictions on data availability

All imaging as well as numerical data relevant to this study are publicly available on the online repository Zenodo (<https://doi.org/10.5281/zenodo.3747143>), or upon reasonable request. All code including adapted STORM-analysis code, TrackFRAP, FRAPTA and other Python scripts and Fiji macros for figure generation are

available in the online repository Github (<https://github.com/TimoHenry/MitochondrialRNAgranules>), or upon reasonable request. Plasmids and cell lines are available to share, do not hesitate to contact the corresponding authors should you have any further enquiries.

Field-specific reporting

Please select the one below that is the best fit for your research. If you are not sure, read the appropriate sections before making your selection.

Life sciences Behavioural & social sciences Ecological, evolutionary & environmental sciences

For a reference copy of the document with all sections, see [nature.com/documents/nr-reporting-summary-flat.pdf](https://www.nature.com/documents/nr-reporting-summary-flat.pdf)

Life sciences study design

All studies must disclose on these points even when the disclosure is negative.

Sample size	No hypothesis-based experiment was performed. Therefore, the sample size was not predetermined. Sample sizes were chosen based on the distribution of the data-points. For morphology data, we collected images and quantified the features within. We then plotted histograms of the feature properties, and ensured that the sample sizes were large enough that the distribution was well-sampled. For FRAP data, experiments were performed in triplicate. Sample size was based on experience in prior studies and sized to allow significance in biologically relevant effect sizes.
Data exclusions	STORM data acquisition was stopped on a case-by-case basis. E.g. when STORM-buffer exceeded its optimal capacity and dye blinking diminished. SMLM data were also filtered for quality using common metrics in the field (number of localizations, sigma). Out of focus data was excluded. These are standard procedures in the field. For live imaging, data with visual deterioration of cellular health were excluded. Loss of focus also led to exclusion of FRAP FOVs. These are standard procedures in the field. Exclusion of data can be retraced through metadata of filters applied.
Replication	Multiple replicates were performed with each antibody and the staining results were in general reproducible. Stained samples that did not show the expected localization to mitochondria were excluded, and often could be attributed to using previously prepared, rather than fresh, solutions. BrU-IF is particularly sensitive to rigorous adherence to published protocols. Replicate samples prepared in parallel yielded comparable results, confirming that the variability was due to sample preparation and not intrinsic variability. All experiments presented in the paper have been reproduced multiple times (a minimum of three replicates), except the correlative light and electron microscopy, as indicated in the manuscript. To ensure reproducibility, we carefully controlled the experimental conditions (passages of cells, stable cells to control expression levels, etc.). All attempts at replication were successful.
Randomization	This is not applicable to our study. Randomization is introduced to reduce bias. There is no risk of bias in our study because all analyses were quantitative, and not subjective.
Blinding	There was not a group allocation component to the study.

Reporting for specific materials, systems and methods

We require information from authors about some types of materials, experimental systems and methods used in many studies. Here, indicate whether each material, system or method listed is relevant to your study. If you are not sure if a list item applies to your research, read the appropriate section before selecting a response.

Materials & experimental systems

n/a	Involvement in the study
<input type="checkbox"/>	<input checked="" type="checkbox"/> Antibodies
<input type="checkbox"/>	<input checked="" type="checkbox"/> Eukaryotic cell lines
<input checked="" type="checkbox"/>	<input type="checkbox"/> Palaeontology
<input checked="" type="checkbox"/>	<input type="checkbox"/> Animals and other organisms
<input checked="" type="checkbox"/>	<input type="checkbox"/> Human research participants
<input checked="" type="checkbox"/>	<input type="checkbox"/> Clinical data

Methods

n/a	Involvement in the study
<input checked="" type="checkbox"/>	<input type="checkbox"/> ChIP-seq
<input checked="" type="checkbox"/>	<input type="checkbox"/> Flow cytometry
<input checked="" type="checkbox"/>	<input type="checkbox"/> MRI-based neuroimaging

Antibodies

Antibodies used

Antibodies used are commercially available and referenced in the main manuscript. Please refer to materials and methods section for more information. anti-FASTKD2 (Proteintech, 17464-1-AP), anti-bromodeoxyuridine (Roche, 11170376001), anti-GRSF1 (Sigma, HPA036985), anti-DNA (ProGen, 61014), anti-TOMM20 (Abcam, ab186734; Santa Cruz Biotech., SC-17764), anti-Complex IV (Thermo Fisher Scientific, A21348), anti-Hsp70 (Thermo Fisher Scientific, MA3-028), anti-GRSF1 (Sigma, HPA036985), anti-FASTKD5 (Sigma, SAB2700438), anti-TFAM (Proteintech, 22386-1-AP), anti-mtSSB (Proteintech, 12212-1-AP), anti-PHB (Thermo Fisher Scientific, MS-261-PO), anti-OxPhos Complex IV subunit IV (clone 20E8C12, Thermo Fisher Scientific, A21348), anti-PDHE1 α (GeneTex, GTX104015)

Validation

Dilution for STORM imaging: 1:200 or 1:250 for primary antibodies & 1:500 - 1:1000 for secondary antibodies
 Dilution for Western blots: All primary antibodies were diluted 1:2000
 Dilution for fluorescence imaging: 1:200 - 1:500 for primary antibodies & 1:500 - 1:1000 for secondary antibodies

- **Proteintech:** We use affinity chromatography, which makes use of the binding strength of a protein for its ligand. Another popular method is protein A/G purification, which uses the recombinant fusion protein A/G from *E. coli*. Protein A/G purification will yield all IgGs in the serum, not just the desired antibodies. Affinity chromatography selects for just the ones with the highest affinity toward the target. We also validate our antibodies through knockout and knockdown (KO/KD) studies. Proteintech was the first company to implement siRNA knockdown validation experiments, the gold standard for testing antibody specificity. The validation process involves using small interfering RNA to knock down gene expression in an antibody product – assessing whether the signal subsides with the expression of the target gene.

1. anti-FASTKD2 (Proteintech, 17464-1-AP): for WB, IP, IHC, IF, ELISA (used in our study for WB, IF)
species specificity: human, mouse, rat, zebrafish
2. anti-TFAM (Proteintech, 22586-1-AP): for WB, IP, IHC, ELISA (used in our study for WB)
species specificity: human, mouse, chicken
3. anti-mtSSB (Proteintech, 12212-1-AP): for WB, chIP, IF, ELISA (used in our study for WB)
species specificity: human, mouse, rat

- **Sigma:** Prestige Antibodies® are highly characterized and extensively validated antibodies with the added benefit of all available characterization data for each target being accessible via the Human Protein Atlas portal linked just below the product name at the top of this page. The uniqueness and low cross-reactivity of the Prestige Antibodies® to other proteins are due to a thorough selection of antigen regions, affinity purification, and stringent selection. Prestige antigen controls are available for every corresponding Prestige Antibody and can be found in the linkage section. Every Prestige Antibody is tested in the following ways:
 - IHC tissue array of 44 normal human tissues and 20 of the most common cancer type tissues.
 - Protein array of 364 human recombinant protein fragments.
 - Validated for multiple commonly used applications such as IHC (Immunohistochemistry), IF (Immunofluorescence), and WB (Western Blot)

1. anti-GRSF1 (Sigma, HPA036985): also validated by orthogonal RNAseq; validated for: WB, IF, IHC (used in our study for WB)
species specificity: human

2. anti-FASTKD5 (Sigma, SAB2700438):
for: WB, IHC (used in our study for WB)
species specificity: human

3. anti-bromodeoxyuridine (Sigma/Roche, 11170376001/BMC9318)
The antibody specifically binds to bromodeoxyuridine and crossreacts with iodouridine (10%). Anti-bromo-deoxyuridine does not crossreact with fluorodeoxy-uridine, nor with any endogenous cellular components such as thymidine or uridine.
For: FC, IHC/IF, cryosections, paraffin sections (used in our study for IF)
Produced in mice, general species specificity

- **ProGen:**
Purified by size exclusion chromatography and validated in publications by WB, IHC since 1986.
anti-DNA (ProGen, 61014)
for: ICC, IF, IHC (used in our study for IF)
species specificity: all

- **Abcam:**
Produced recombinantly (animal-free) for high batch-to-batch consistency and long-term security of supply.
anti-TOMM20 (Abcam, ab186734)
for: FC, ICC, IF, IHC, WB (used in our study for IF)
species specificity: mouse, rat, human

- **Santa Cruz Biotech:**
Validated by knockdown + WB, and by WB, IF, etc in >300 publications.
anti-TOMM20 (Santa Cruz Biotech., SC-17764)
for: IP, ELISA, IF, IHC, WB (used in our study for IF)
species specificity: mouse, rat, human

- **Thermo Fisher Scientific:**
anti-Complex IV (Thermo Fisher Scientific, A21348)
Validated by knockdown + WB
for: ELISA, ICC, IF, IHC, WB (used in our study for WB)
species specificity: mouse, rat, human

anti-Hsp70 (Thermo Fisher Scientific, MA3-028)
MA3-028 has been successfully used in Western blot, immunocytochemical, immunofluorescence, immunohistochemical (paraffin), and immunoprecipitation procedures. It has been thoroughly tested and validated for cellular immunofluorescence (IF) applications.
for: ELISA, ICC, IF, IHC, WB (used in our study for WB)
species specificity: mouse, rat, human

anti-PHB (Thermo Fisher Scientific, MS-261-PO)
Validated by knockdown + WB
for: ELISA, ICC, IF, IHC, WB (used in our study for WB)
species specificity: mouse, rat, human, pig, chicken

anti-OxPhos Complex IV subunit IV (clone 20E8C12, Thermo Fisher Scientific, A21348)
 Validated by knockdown + WB
 for: ELISA, ICC, IF, IHC, WB (used in our study for WB)
 species specificity: mouse, rat, human, chimpanzee, non-human primate, yeast

• GeneTex:
 Validated by knockout + WB
 anti-PDHE1 α (GeneTex, GTX104015)
 for: ICC, IF, IHC, WB (used in our study for WB)
 species specificity: mouse, rat, human

Eukaryotic cell lines

Policy information about [cell lines](#)

Cell line source(s)

COS7 - ECACC - 87021302
 HEK293T - ATCC - CRL-11268
 HeLa - ATCC - CCL-2
 U2OS - ATCC - HTB-96

Authentication

ATCC, the provider of U2OS and HeLa cell lines, uses STR profiling for authentication.
 ECACC, the provider of the HEK293T cell line, uses STR profiling for authentication.
 HPA culture collections, the provider of the COS7 cell line, operates in tandem with ECACC and uses STR profiling for authentication.

Mycoplasma contamination

FACSeD cell lines were tested for mycoplasma contamination with negative results. Mycoplasma contamination was checked for routinely in all cell lines.

Commonly misidentified lines
 (See [ICLAC](#) register)

Not applicable as no commonly misidentified cell lines were used in the study.